IEEE Access
Multidisciplinary | Rapid Review | Open Access Journal

Date of publication xxxx 00, 0000, date of current version xxxx 00, 0000.

Digital Object Identifier 10.1109/ACCESS.2017.DOI

Distributed sensing via inductively coupled single-transistor chaotic oscillators: a new approach and its experimental proof-of-concept.

LUDOVICO MINATI[1,2], (Senior Member, IEEE), KORKUT KAAN TOKGOZ[3], (Member, IEEE), MATTIA FRASCA[4], (Senior Member, IEEE), YASUHARU KOIKE[5], JACOPO IANNACCI[6], NATSUE YOSHIMURA[5,7], KAZUYA MASU[8], (Member, IEEE), HIROYUKI ITO[5], (Member, IEEE)

[1]Tokyo Tech World Research Hub Initiative (WRHI), Institute of Innovative Research, Tokyo Institute of Technology, Yokohama 226-8503, Japan
[2]Center for Mind/Brain Science (CIMeC), University of Trento, Trento 38123, Italy
[3]Research Center for Earth Inclusive Sensing, Tokyo Institute of Technology, Yokohama 226-8503, Japan
[4]Dept. of Electrical, Electronic and Computer Engineering (DIEEI), University of Catania, Catania 95125, Italy
[5]FIRST, Institute of Innovative Research, Tokyo Institute of Technology, Yokohama 226-8503, Japan
[6]Center for Materials and Microsystems (CMM), Fondazione Bruno Kessler (FBK), Trento 38123, Italy
[7]PRESTO, JST, Saitama 332-0012, Japan
[8]Tokyo Institute of Technology, Tokyo 152-8550, Japan

Corresponding author: Ludovico Minati (e-mail: minati.l.aa@m.titech.ac.jp, lminati@ieee.org).

ABSTRACT Emerging applications across environmental, biomedical, and structural monitoring require the measurement of physical variables over extended regions. Because addressing many sensors individually can result in impractical bandwidth and power requirements, there is a need for distributed sensing approaches wherein readouts are obtained directly at the ensemble level. In turn, this generally requires sensor nodes capable of interacting with each other to implement the required readout statistic. Here, the first practical steps towards approaching this challenge via a nonlinear analog approach based on chaotic synchronization are presented. Namely, single-transistor oscillators, representing remarkably low-complexity yet highly-flexible entities, are experimentally found to be suitable for wireless coupling via mutual induction, realizing a simple form of telemetry for luminous flux. Via numerical simulations and numerous laboratory experiments, a rich repertoire of possible interactions among multiple sensor nodes and between the same and an external exciter is demonstrated, encompassing synchronization, desynchronization, relay effects, and chaotic transitions. Together, these results reveal the possibility and means of accurately estimating the average of a distributed physical magnitude from the complexity of ensemble dynamics. This new approach contributes an important blueprint for future work using simple chaotic circuits in sensing applications.

INDEX TERMS Chaos, Chaotic oscillator, Correlation dimension, Distributed sensing, Entropy, Inductive coupling, Remote measurement, Synchronization, Transistor oscillator, Telemetry, Wireless network.

I. BACKGROUND AND INTRODUCTION

A. DISTRIBUTED SENSING

Over the last two decades, automation has undergone a profound transformation towards ever more distributed paradigms wherein, instead of controlling separate processes based on input from individual sensors, control systems are increasingly used to manage complex systems and networks [1]–[3]. An indispensable ingredient for this evolution is, and has been, the ability to gather data from multiple sensors scattered over a structure, surface, or environment. In turn, this ability has principally been provided by the development of wireless sensor network technologies, which alleviate the cost and physical overheads associated with laying extensive or dense wired connections. To date, these networks constitute a topic of intensive research, targeted at core issues such as over-the-air timing synchronization, as well as the optimization of bandwidth and power budgets, which are often the limiting factors in real-world scenarios. Their

This article has been accepted for publication in a future issue of this journal, but has not been fully edited. Content may change prior to final publication. Citation information: DOI 10.1109/ACCESS.2020.2976139, IEEE Access

predominant applications are in agriculture, meteorology, air quality monitoring, and biomedicine [4]–[7].

Arguably, the most established instances of "distributed sensing" are presently realized using specially-designed fiber optics, which generate a back-scattering signal tracking in a calibrated manner a physical variable such as temperature or the concentration of an analyte. In this context, time- and frequency-domain techniques allow reconstructing a one-dimensional measurement profile along the fiber length. Aside from the high cost due to the advanced optoelectronic devices required, these technologies are inherently poorly suited for applications requiring pervasive monitoring, or minimum intrusiveness [8], [9]. On the other hand, existing wireless sensor networks generally hinge around a one-to-many communication scheme, wherein a limited number of base-stations individually address (or passively receive from) a large number of nodes. This requires a considerable aggregate bandwidth, translating into the need for complex radio-frequency infrastructure, potentially requiring transceivers that are difficult to power purely based on harvesting techniques such as solar cells. Ad-hoc networks can mitigate this problem but still imply significant hardware and software complexity [10], [11].

B. PARAMETRIC MAPPING VS. SUMMARY STATISTICS

In many applications, a full topographical mapping is not continuously necessary, and a summary statistic, such as average, sum, or extrema values, is sufficient for ongoing monitoring, enabling the triggering of more detailed data gathering and inference only when an anomaly is detected. In such scenarios, a drastic data reduction is performed during analysis, rendering it wasteful to transfer data from each sensor in the first place: it would be more efficient if the network itself could, collectively, calculate the summary statistic by a form of consensus.

One example application would be the monitoring of concrete pillars: assuming hundreds or thousands of "smart dust" sensors are embedded in the mixture, the challenge would be to seamlessly quantify the overall structural degradation, i.e., sum the number of micro-fissures. Another possible application would be in precision agriculture: assuming sensors are equipped with biochemical transducers able to measure the presence of a parasite, the purpose of the monitoring would be to detect the highest or average concentration in a field. In both cases, a distributed computation of the summary statistic, performed continuously at low power draw, would reduce the complexity of "middleware" infrastructure. Further, there would be substantial practical advantages if the state of the network as a whole, reflecting the variable to be measured, could be inferred based on signals received from a small subset of it, thus reducing the communication range requirements [10]–[14].

In order to implement the distributed calculation of a summary statistic, it is needed for sensor nodes to interact among themselves, engendering a purposeful collective behavior, which could, for instance, be in the form of synchronized dynamics. This requirement is closely related to the approach of "autonomic computing" or intelligent networks, wherein nodes can self-organize, realizing in an emergent manner not only computation but also recovery and optimization functions [3], [15], [16].

C. COUPLED NONLINEAR OSCILLATORS

Because it requires substantial interaction, self-organization may translate into a high power consumption when it is implemented digitally, due to computing and transceiver load. An innovative approach would be to elicit it in the analog domain, for example, via coupled oscillators. Thus far, in the field of wireless sensor networks, coupled oscillators have been considered almost exclusively regarding pulse coupling schemes aiming to provide robust frequency distribution; nevertheless, it is known from biological models that nonlinear oscillators can also give rise to complex emergent phenomena [1], [17]–[20]. With that in mind, in the present work, we investigate the possibility of taking the degree of dynamical complexity in partially-synchronized network activity as a means of obtaining a distributed measurement of a physical variable. We demonstrate a number of network phenomena having direct relevance for this purpose.

It is well-established that nonlinear oscillators, mainly when operating in or close to chaotic mode, can realize complex operations, including forming emergent spatiotemporal patterns such as clusters (or communities), stationary and traveling waves, even instances of remote entrainment [21]–[25]. At its simplest, an electronic chaotic oscillator can be realized through a bipolar junction transistor, whose transfer function provides both the amplification and the nonlinearity. Notably, a rich spectrum of dynamical behaviors can arise under diverse arrangements comprising a single transistor, two inductors, one capacitor, and one control resistor. Recently, it was suggested that networks of these circuits, coupled diffusively in elementary topologies such as rings or lattices or more complicated configurations, can be used as a basis to realize emergent collective behaviors via chaotic synchronization [26]–[30].

Yet, at present, only minimal research has been conducted on the synchronization of these oscillators at a distance without an electrical collection, limited to two studies on the Colpitts circuit: one measuring a magnetically coupled pair, and another simulating a light coupling scheme [31], [32]. Realistic studies similar to those available for wirelessly coupled oscillators with a frequency distribution such as Ref. [33] are lacking.

D. CONTRIBUTION

In this paper, we experimentally demonstrate for the first time the possibility of realizing the core mechanisms necessary for distributed sensing via chaotic synchronization. Namely, we implemented it in a network of inductively coupled single-transistor chaotic oscillators powered by photovoltaic cells. We show the occurrence of chaotic transitions, synchronization, the interaction with an external field and confirm the

This article has been accepted for publication in a future issue of this journal, but has not been fully edited. Content may change prior to final publication. Citation information: DOI 10.1109/ACCESS.2020.2976139, IEEE Access

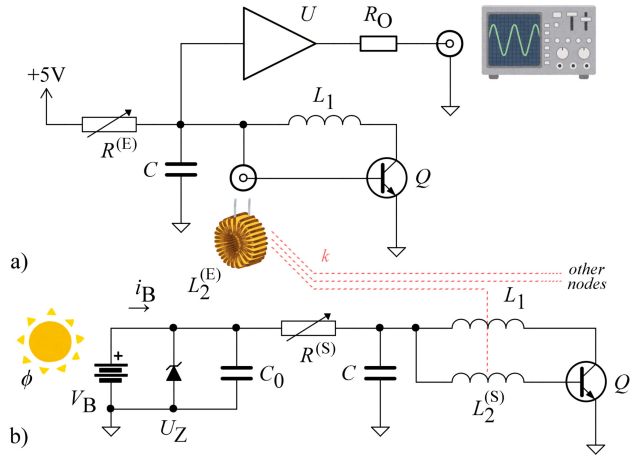

FIGURE 1. Schematics of the physically-realized circuits. a) Exciter node (E); $L_2^{(E)}$ denotes the externally-connected wire-loop coupling coil, U and R_O represent the output buffer towards an oscilloscope. b) Sensor node (S); voltage V_B at current i_B corresponds to the photovoltaic cell illuminated with a light source having flux ϕ or to an external source, U_Z and C_0 implement over-voltage protection and bypassing, $L_2^{(S)}$ denotes the printed coil, coupled to $L_2^{(E)}$ with coefficient k. Components C, L_1 and Q are nominally equal for all circuits, whereas $R^{(E)}$ and $R^{(S)}$ represent the individually-tuned parameters controlling the node dynamics. Depending on the configuration, each exciter may be coupled to more than one sensor, and multiple sensors may be coupled between themselves.

possibility of accurately estimating the global light intensity from the dynamical complexity characterizing the collective oscillation.

In Section II, the circuit of interest is firstly presented from the practical viewpoint of its realization and the associated experimental setup. In Section III, aspects of the underlying theory are provided with reference to numerical simulations of an elementary model capturing the essential dynamical features. In Section IV, an extensive series of experimental results is reported, firstly about the effects of coupling then about the sensed variable. Finally, in Section V, the implications of the observed phenomena are considered, and directions for future applications of a new approach to distributed sensing are proposed.

II. CIRCUITS AND MEASUREMENTS

A. OSCILLATOR DESIGN, REALIZATION AND COUPLING

Each node comprised one autonomous oscillator, consisting of a single NPN bipolar-junction transistor in a common-emitter configuration, whose base and collector terminals are connected via separate inductors to a grounded capacitor and a variable resistor towards a DC voltage source (Fig. 1). Despite its elementary form, this arrangement was discovered only recently, and remarkably found to generate a multitude of chaotic behaviors, including spiral, funnel, phase-coherent and Rössler-like attractors; in a realization wherein the inductors are replaced with fractal resonators, this circuit is also capable of producing high-dimensional dynamics [30], [34]. Chaos arises due to nonlinear interaction between the currents in the two inductors via the transistor; furthermore, there is an interplay between oscillations at the frequencies determined by the L-C pairs, corresponding not only to the discrete capacitor but also to the junction capacitance at the collector. By moving the operating point of the transistor, the series resistor shapes the nonlinearity: as such, it acts as the primary control parameter, depending on which chaotic transitions can be observed. In these experiments, it was generally tuned to obtain operation close to an order-chaos transition [30], [34].

The experiments in the present study revolved around two structurally coincident realizations of this oscillator. The first, dubbed `ame` (雨, rain), served as "exciter" (E) for one or a multitude of sensor nodes which were inductively coupled to it. In other words, it provided access to a signal reflecting the dynamical activity of the network, not in a passive manner (as a simple receiver would) but via actively synchronizing with it, that is, exchanging energy bidirectionally [26]. In this circuit, the inductor attached to the base of the transistor was constructed as a wide-field coil. It shared a small fraction of its magnetic flux with the corresponding coils in the collective of sensor nodes. Power was provided externally, and a low-capacitance buffer drove a transmission line towards a digitizing oscilloscope (Fig. 1a). The second, dubbed `tsubomi` (蕾, bud), implemented a sensor node (S), wherein the inductor attached to the transistor base was also a coupling coil, but one featuring a considerably narrower field. Mimicking a representative use scenario, power for these nodes was provided by photovoltaic cells, and no external electrical connections were necessary (Fig. 1b).

In both nodes, the transistor Q was of type 2SC5226A (ON Semiconductor Inc., Phoenix AZ). The fixed inductors and capacitors had nominal values $L_1 = 220$ μH (type NLFV32T-221K-EF; TDK Corp., Tokyo, Japan) and $C = 270$ pF (type CC0603JRNPO9BN271; Yageo Corp., New Taipei City), and the variable resistors had values $R^{(E,S)} \in [0, 2000]$ Ω. For the exciter node (E), the buffer was of type MAX4201 (Maxim Integrated Inc., San Jose CA), with $R_O = 50$ Ω; the supply voltages to the oscillator and buffer were, respectively, 5 V and ± 6 V. For the sensor node (S), the photovoltaic source consisted of three monocrystalline cells (type KXOB22-04X3F; IXYS Corp., Milipitas CA) connected in series, providing an open-circuit voltage V_B up to $U_Z = 6.2$ V limited by a Zener diode (type CZRU52C6V2; Comchip Technology Corp., New Taipei City). The high-frequency source impedance was lowered through two low-ESL parallel bypassing capacitors having a total value of $C_0 = 9.4$ μF (type LWK212BJ475KD; Taiyo Yuden Corp., Tokyo, Japan). Importantly, all components were subject to fabrication tolerances, which rendered the nodes nonidentical: these were on the order of $\pm 10\%$ for L_1 and L_2, $\pm 5\%$ for C and the setting of R, and $\pm 20\%$ for the transistor parameters and the photovoltaic cell voltage V_B.

The circuits were physically realized on separate two-layer printed circuit boards, both types having size 32×32 mm,

This article has been accepted for publication in a future issue of this journal, but has not been fully edited. Content may change prior to final publication. Citation information: DOI 10.1109/ACCESS.2020.2976139, IEEE Access

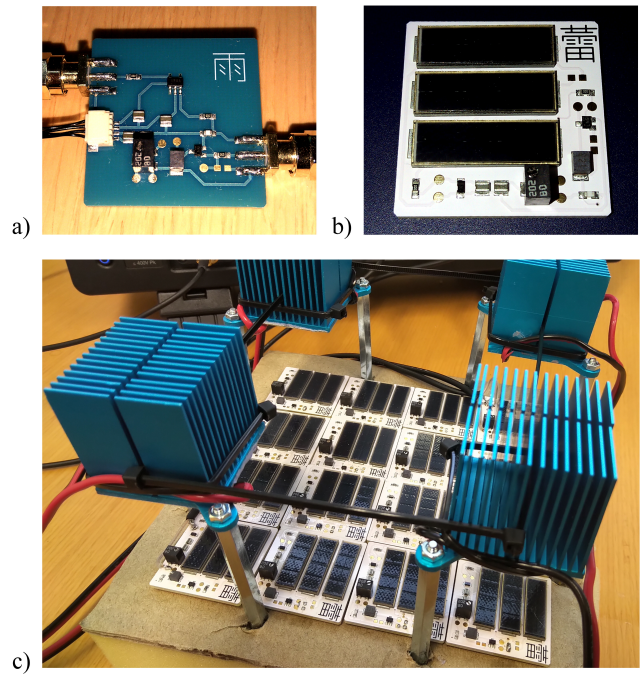

FIGURE 2. Circuit boards and arrangement. a) Exciter node (E); left-side connectors are for power input and signal output, right-side connector is towards the wire-loop coupling coil. b) Sensor node (S), whose area is largely covered by the photovoltaic cells. c) Representative arrangement of 4×4 sensor nodes illuminated by four LEDs located at the corners (underneath the blue heat-sinks).

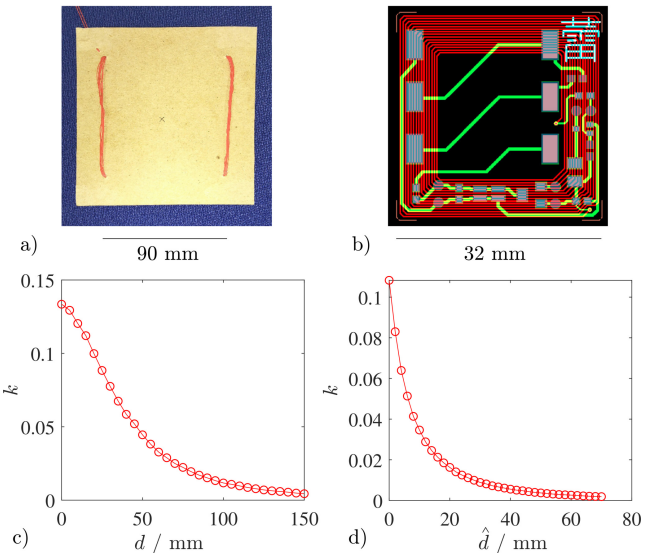

FIGURE 3. Coupling coils. a) Wide-field coil realized as a wire loop on a cardboard support and connected to the exciter node (E). b) Flat coil with square winding printed onto the underside of each sensor node board (S). Experimentally-measured coupling coefficient k as a function of c) the distance d between the wire-loop and one printed coil, (E)-(S), and d) the spacing $\hat{d}$ between two printed coils, (S)-(S).

whose fabrication files are publicly available [35]. In the exciter node, SMA connectors were provisioned for interfacing to the wide-field coil and oscilloscope (Fig. 2a). In the sensor node, there were no connectors; however, test-points were provided for external voltage supply and measurement during some of the experimental sessions (Fig. 2b). The coupling coils for the two circuits were designed in such a manner as to reproduce a situation of weak coupling over a scale of distances convenient for laboratory measurement conditions while allowing a multitude of topographical arrangements. Namely, the wide-field coil connected to the exciter node consisted of 8 turns of single-core wire having a diameter of 0.25 mm along the perimeter of a 90 mm square (Fig. 3a). In contrast, the flat coil for the sensor node was embedded in the solder copper side of its printed circuit board, covering the outer area and arranged as a square concentric pattern with 15 turns of a 0.2 mm-wide track with 0.2 mm spacing, thickness 35 μm (Fig. 3b).

At $f = 2$ MHz, approximately corresponding to the centroid of the oscillation spectrum, their inductances respectively measured $L_2^{(\mathrm{E})} = 21$ μH and $L_2^{(\mathrm{S})} = 10$ μH (type E4991A; Keysight Inc., Santa Rosa CA); as shown in Ref. [30], these values are not critical for obtaining chaos. Considering one wide-field coil and one sensor node coil directly overlaying its center, the coupling coefficient, measured at $Z_0 = 50$ Ω via a signal generator and oscilloscope (type WS3054; Teledyne LeCroy Inc., Chestnut Ridge NY), gradually decayed as $k \approx \{0.14, 0.04, 0.01, 0.004\}$ at distances $d = \{0, 50, 100, 150\}$ mm (Fig. 3c). For two coplanar sensor coils linearly displaced along one axis from each other, the coupling coefficient decayed as $k \approx \{0.11, 0.02, 0.005, 0.003\}$ at spacings $\hat{d} = \{0, 20, 40, 60\}$ mm (Fig. 3d). These values are comparable to those which can be observed over considerably larger distances, suitable for real-world applications, when suitably scaled coils are used, and to the configuration considered in the preexisting study on magnetically coupled Colpitts oscillators [31], [36].

B. DATA ACQUISITION AND ANALYSIS

The interactions between the exciter and sensor node(s), and among the sensor nodes themselves, were evaluated for several different arrangements, which are detailed in Sec. IV; in brief, the influence of distance and spacing was measured while powering the sensor(s) with a fixed external voltage, whereas the effect of light intensity was assessed while illuminating their photovoltaic cells with high-intensity LED arrays (Fig. 4).

All measurements were conducted in a shielded enclosure; they were repeated and averaged between 3-5 times, depending on the experiment, to confirm consistency and attenuate random error. Time-series of one million points were recorded at 1 GSa/s using a digitizing oscilloscope (type WS3054; Teledyne LeCroy Inc.), separately for all experimental conditions under the control of scripts written in the Matlab language (MathWorks Inc., Natick MA). The raw data are freely downloadable from Ref. [35]. When acquiring directly from sensor nodes, low-capacitance probes

were used to record the capacitor voltage $v_C(t)$, which was elected as the physical state variable of interest and, where appropriate, the supply voltage V_B. All acquisitions were performed in AC coupling mode, and a-posteriori smoothing was performed to reduce analog-to-digital conversion discretization effects. Software-controlled illumination was provided by four independent high-current white LED arrays (type CMA3090; Cree Inc., Durham NC), each emitting a luminous flux up to $\phi_\mathrm{max} = 12400$ lm; these were positioned at a fixed distance over either single sensors or an array of 4×4 sensors (Fig. 2c). Their intensity was controlled via dimmable power supplies (type HBG-100-48B; Mean Well Inc., Fremont CA) controlled by an Arduino UNO board (Interaction Design Institute, Ivrea, Italy).

Off-line analyses were performed, aiming to quantify the level of dynamical complexity as well as synchronization between the nodes in each configuration. Firstly, a measure of attractor fractality, namely the correlation dimension D_2, was computed. To this end, phase-space reconstruction was performed based on time-delay embedding, with $\boldsymbol{x}(t) = [x(t-\delta t(m-1)), x(t-\delta t(m-2)), \ldots, x(t)]$ [37] setting, as customary, the embedding lag δt equal to the first local minimum of the time-lag mutual information function [38], the embedding dimension m as the lowest integer number for which $< 5\%$ of false nearest neighbors are observed [39], and the minimum neighbor time separation (Theiler window w) to twice the first local maximum on the space-time separation plot [40]. These analyses were carried out using the `TISEAN` package (ver. 3.0.1) [41]. Based on this time-lag embedding, D_2 was estimated via the Grassberger-Procaccia method, namely from the correlation sum

$$C(m,\epsilon) = \frac{1}{N_\mathrm{pairs}} \sum_{j=m}^{N} \sum_{k<j-w} \Theta(\epsilon - |\boldsymbol{x}_j - \boldsymbol{x}_k|) \quad (1)$$

where $N_\mathrm{pairs} = (N-m+1)(N-m-w+1)/2$ denotes the number of point pairs covered by the sums, and $\Theta(x)$ is the Heaviside step function [42]. Insofar as the embedding dimension m exceeds the box-counting dimension of the underlying attractor, over sufficiently small length scales ϵ, one has

$$C(m,\epsilon) \propto \epsilon^{D_2} \,. \quad (2)$$

Here, over-embedding was performed up to $2m$, calculations were performed in each recording for 10 evenly-spaced segments of 50,000 points, and the convergence plateau of D_2 in m, ϵ was estimated via a direct search method introduced previously [29], [30]. While this estimator tends to be negatively biased in the presence of high-dimensional signals, it was deemed adequate given the relatively low-dimensional dynamics expected in these experiments [43].

A further complexity measure, based on information theory rather than dynamics, was also applied. Namely, the permutation entropy is a non-parametric technique, which only considers an ordinal representation of the temporal evolution in a signal; as such, it is particularly robust to noise, discretization, and other issues that often affect experimental datasets. To apply this method, the dynamics $x(t)$ were transformed to a map-like representation by extracting the sequences of local extrema points, identified through $\dot{x}(t) = 0$, with either $\ddot{x}(t) < 0$ and $x(t) \geq x(t \pm \delta t)$ or $\ddot{x}(t) > 0$ and $x(t) \leq x(t \pm \delta t)$, wherein $\delta t = 20$ ns. This yielded a step-wise amplitude time-series having length l; such a representation has been shown to successfully capture the cycle amplitude fluctuation dynamics occurring in this circuit [34]. In brief, the dynamics are encoded by ranks, meaning, based on the symbolic sequences of ascending and descending values. Insofar as the phase space bin counts are sufficiently large to be statistically representative, the permutation entropy is given by

$$H = -\sum_{j}^{m!} p_j \log_2 p_j \,, \quad (3)$$

wherein p_j denote the relative symbol frequencies. Usually, H is normalized, giving $h = H/\log_2 m! \in [0,1]$ [44]. The order (sequence length) was set to $m = 6$ (not critical), ensuring that the coverage criterion $5m! < l$ was in most cases met [45].

Synchronization was estimated in terms of phase locking, which is a robust hallmark of entrainment between chaotic oscillators [26]. To this end, for each pair of experimental time-series $x_j(t)$ with $j = 1, 2$, the analytic signals were calculated

$$\psi_j(t) = x_j(t) + i\tilde{x}_j(t) = A_j(t)e^{i\varphi_j(t)} \,, \quad (4)$$

where $i = \sqrt{-1}$, $\tilde{x}_j(t)$ denotes the Hilbert transform of $x_j(t)$

$$\tilde{x}_j(t) = \frac{1}{\pi}\mathrm{p.v.}\left[\int_{-\infty}^{\infty} \frac{x_j(\tau)}{t-\tau}\mathrm{d}\tau\right] \,, \quad (5)$$

and where p.v. represents the Cauchy principal value of the integral. The instantaneous relative phase is then

$$\Delta\varphi(t) = \arg[\psi_j(t)\overline{\psi}_k(t)] \,, \quad (6)$$

from the distribution of which the corresponding phase-locking value can be obtained as

$$r = |\langle e^{i\Delta\varphi(t)}\rangle_t| \,. \quad (7)$$

III. THEORY AND SIMULATIONS

As introduced in Section I.C, the approach presented in this study is founded on several universal concepts from the theory of nonlinear dynamical systems and networks. One fundamental notion is that of chaotic transitions, that is, the ability of isolated as well as coupled nonlinear oscillations to seamlessly transition between periodic and chaotic behavior. This can ensue as a function of an arbitrary control parameter (such as coupling, or a physical variable to be sensed) and involve diverse mechanisms, including bifurcations and quasiperiodicity. Another notion is that of synchronization, that is, the ability to entrain oscillators which are possibly

This article has been accepted for publication in a future issue of this journal, but has not been fully edited. Content may change prior to final publication. Citation information: DOI 10.1109/ACCESS.2020.2976139, IEEE Access

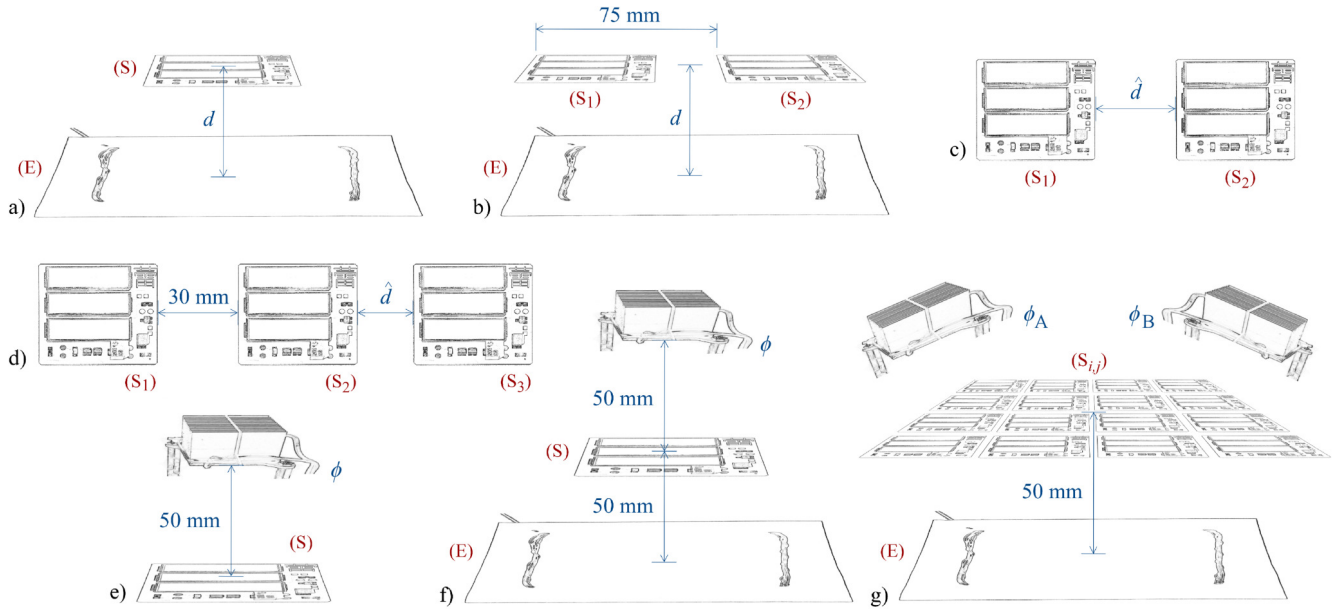

FIGURE 4. Board arrangements in the experiments measuring a) Effect of the distance d between the wire-loop coil (E) and one sensor board (S) above it, b) Effect of the distance d between the wire-loop coil (E) and two co-planar sensor boards (S_1), (S_2) above it, c) Effect of the spacing $\hat{d}$ between two isolated co-planar sensor boards (S_1), (S_2), d) Effect of the spacing $\hat{d}$ between two co-planar sensor boards (S_2), (S_3) located next to a fixed sensor board (S_1), e) Effect of the luminous flux ϕ on an isolated sensor board (S), f) Effect of the luminous flux ϕ on a sensor board (S) located at a fixed distance above the wire-loop coil (E), g) Effects of the distance d, luminous flux ϕ_u and other interventions on a 4×4 array of sensor nodes ($S_{i,j}$), located above the wire-loop coil (E).

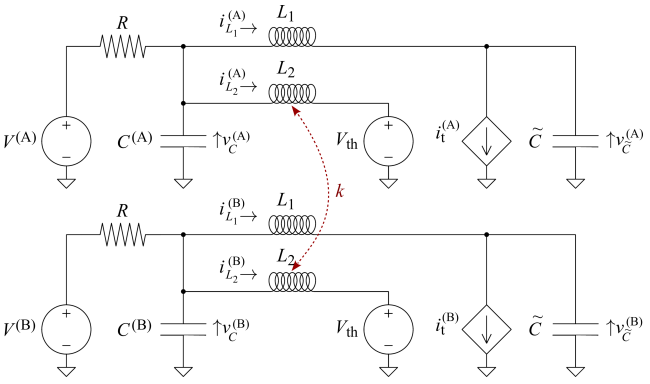

FIGURE 5. Simplified circuit representing two coupled oscillators in the numerical simulations, wherein each transistor Q is replaced by a constant voltage source V_{th}, a nonlinear controlled current source $i_{\mathrm{t}}^{(\mathrm{A})}$ or $i_t^{(\mathrm{B})}$, and a parasitic capacitance $\tilde{C}$.

rendered nonidentical by small or large mismatches, generating stable phase relationships (locking). Notably, synchronization and chaotic transitions are related in various aspects. Coupling two systems may result in their synchronization, if the energy transfer rate is sufficiently high, with higher levels required for synchronizing chaotic than periodic dynamics. At the same time, depending on the specific configuration, coupling may cause a transition towards chaos or periodicity; in the presence of mismatches, increased coupling strength often promotes transition to chaos [22], [26], [46].

While a detailed presentation of these concepts is omitted for brevity, the main phenomena are exemplified in this section, via three idealized scenarios. These are numerically simulated to support the interpretation of the experimental results which follow. Previous theoretical work on the chosen transistor circuit has shown that, upon consideration of the oscillation dynamics and associated circuit variables, it is possible to reproduce the qualitative features of individual and collective behavior while reducing the transistor equations as follows [34], [47]. Firstly, the base-emitter junction is represented by a DC voltage source $V_{\mathrm{th}} = 0.6\,\mathrm{V}$; this is acceptable because the base-emitter voltage v_{BE} remains approximately constant. Secondly, the junction capacitances are collapsed into a fixed capacitor $\tilde{C} = 1\,\mathrm{pF}$ between collector and ground; despite its relatively small value, this capacitor is essential for sustaining oscillation (details not shown). Thirdly, the collector-emitter current is captured by a nonlinear current source controlled by the base current i_{B} and collector voltage $v_{\tilde{C}}$ according to

$$i_{\mathrm{t}} = \alpha\left(i_{\mathrm{B}}, v_{\tilde{C}}\right) \tag{8}$$

where, empirically, one can write

$$\alpha\left(x, y\right) = \beta\Gamma\left(x\right)\tanh\left(y/2V_{\mathrm{th}}\right)\ . \tag{9}$$

Here, $\Gamma(x) = x\Theta(x)$, where $\Theta(x)$ is the Heaviside step function, and the corresponding term serves to prevent the amplification of negative base current, while $\tanh(y)$ approximates a step function and implements the nonlinear amplification; the rationale for this simplification and its agreement with more realistic simulations have been clarified previously [34].

This article has been accepted for publication in a future issue of this journal, but has not been fully edited. Content may change prior to final publication. Citation information: DOI 10.1109/ACCESS.2020.2976139, IEEE Access

Predicated on the above, a simplified diagram of an inductively coupled pair of these oscillators is readily obtained (Fig. 5). Applying Kirchhoff's laws one has

$$\begin{cases} \frac{\mathrm{d}v_{C^{(\mathrm{A})}}}{\mathrm{d}t} = \frac{V^{(\mathrm{A})} - v_{C^{(\mathrm{A})}}}{RC^{(\mathrm{A})}} - \frac{i_{L_1^{(\mathrm{A})}} + i_{L_2^{(\mathrm{A})}}}{C^{(\mathrm{A})}} \\ \frac{\mathrm{d}v_{\tilde{C}^{(\mathrm{A})}}}{\mathrm{d}t} = \frac{i_{L_1^{(\mathrm{A})}} - i_{\mathrm{t}}^{(\mathrm{A})}}{\tilde{C}} \\ \frac{\mathrm{d}i_{L_1^{(\mathrm{A})}}}{\mathrm{d}t} = \frac{v_{C^{(\mathrm{A})}} - v_{\tilde{C}^{(\mathrm{A})}}}{L_1} \\ \frac{\mathrm{d}i_{L_2^{(\mathrm{A})}}}{\mathrm{d}t} = \frac{v_{C^{(\mathrm{A})}} - V_{\mathrm{th}}}{L_2} - k\frac{v_{C^{(\mathrm{B})}} - V_{\mathrm{th}}}{L_2} \\ \frac{\mathrm{d}v_{C^{(\mathrm{B})}}}{\mathrm{d}t} = \frac{V^{(\mathrm{B})} - v_{C^{(\mathrm{B})}}}{RC^{(\mathrm{B})}} - \frac{i_{L_1^{(\mathrm{B})}} + i_{L_2^{(\mathrm{B})}}}{C^{(\mathrm{B})}} \\ \frac{\mathrm{d}v_{\tilde{C}^{(\mathrm{B})}}}{\mathrm{d}t} = \frac{i_{L_1^{(\mathrm{B})}} - i_{\mathrm{t}}^{(\mathrm{B})}}{\tilde{C}} \\ \frac{\mathrm{d}i_{L_1^{(\mathrm{B})}}}{\mathrm{d}t} = \frac{v_{C^{(\mathrm{B})}} - v_{\tilde{C}^{(\mathrm{B})}}}{L_1} \\ \frac{\mathrm{d}i_{L_2^{(\mathrm{B})}}}{\mathrm{d}t} = \frac{v_{C^{(\mathrm{B})}} - V_{\mathrm{th}}}{L_2} - k\frac{v_{C^{(\mathrm{A})}} - V_{\mathrm{th}}}{L_2} \end{cases} ; \qquad (10)$$

these equations represent a valid approximation assuming $k \ll 1$, which corresponds to the weak coupling regime of interest in this study and realized through the physically-realized inductors (Fig. 3). Without loss of generality, below let us assume ideal inductors with $L_1 = 220$ μH and $L_2 = 15$ μH; under experimental settings, the nodes are nonidentical, with richer dynamics engendered by parametric mismatches and imperfections such as inductor self-resonance. Further, without loss generality, let us assume a fixed transistor current gain $\beta = 200$ and DC supply voltage $V^{(\mathrm{A,B})} = 2.5$ V. To provide sufficient inter-node variability for avoiding complete synchronization, the capacitor values were drawn randomly in $C^{(\mathrm{A,B})} \in [240, 300]$ pF. The initial conditions were identically set to $v_C(0) = v_{\tilde{C}}(0) = V_{\mathrm{th}}$ and $i_{L_1}(0) = i_{L_2}(0) = V_{\mathrm{th}}/R$. The ODE system was solved up to $t = 15 \times 10^{-5}$ with the Klopfenstein-Shampine method of orders 1-5 for stiff equations, setting a relative tolerance of 10^{-6} [48]. For brevity, permutation entropy results are not presented for these simulations.

Firstly, we evaluated the effect of the coupling coefficient, sweeping it in $k \in [0, 0.2]$, approximately corresponding to the distance ranges between exciter and sensor nodes (E)-(S) and spacings between sensor nodes (S)-(S) considered experimentally (Fig. 3). In these simulations, the series resistance was set to $R = 1000$ Ω, and, aside from the mismatch in their values of C, the two nodes were identical. As $k \to 0.1$, the gradual onset of phase synchronization was well-evident, leading to $k(0.1) \approx 0.9$ (Fig. 6a). In the absence of coupling, the two nodes were initially non-chaotic, with their average correlation dimension $\langle D_2 \rangle \approx 1.1$. As the coupling level was increased, the threshold of $D_2 > 2.0$, generally accepted as a hallmark of chaotic dynamics, was reached already for $k \approx 0.07$; past this point, an inflection was observed, followed by a less marked increase towards a plateau at $\langle D_2 \rangle \approx 2.2$ (Fig. 6b).

Secondly, we considered the effect of sweeping the DC supply voltage at one node (B), with $V^{(\mathrm{B})} \in [0, 5]$ V, effectively electing it as a sensor node and evaluating the impact on the dynamics of the other coupled node (A). In these simulations, the series resistance was set to $R = 1500$ Ω and the coupling coefficient was set to a very low value, namely $k = 0.01$, physically corresponding to a distance $d \approx 100$ mm between exciter and sensor nodes (Fig. 3c) and to a separation $\hat{d} \approx 25$ mm between two sensor nodes (Fig. 3d). A nontrivial influence on synchronization was observed, wherein initially the two nodes were non-synchronized, then a moderate level of phase synchronization ensued between $1.6\ \mathrm{V} < V^{(\mathrm{B})} < 3.6\ \mathrm{V}$ and eventually vanished (Fig. 6c). This pattern was closely reflected in the complexity of the dynamics of the node configured as a sensor, whose supply DC voltage was swept (B), which was highest in the intermediate range of $V^{(\mathrm{B})}$. Of particular importance for possible sensing applications, that voltage had an even more marked effect on the activity of the other, remote, node. Its dynamics were initially periodic, with $D_2^{(\mathrm{A})} \approx 1$, after which the correlation dimension gradually increased, first reaching a plateau $D_2^{(\mathrm{A})} \approx 2.1$ in the vicinity of $V^{(\mathrm{B})} = 2.5$ V and after that increasing further towards $D_2^{(\mathrm{A})} \approx 3.6$ for $V^{(\mathrm{B})} = 5$ V (Fig. 6d).

Thirdly, we simulated a larger scenario consisting of a network of $n = 10$ sensor nodes (S_i, with $i = 1, \ldots, n$), each one receiving a supply voltage $V^{(\mathrm{S}_i)} \in [0, 5]$ V, coupled in an all-to-all configuration between themselves and to an exciter node (E). This situation can be represented as

$$\begin{cases} \frac{\mathrm{d}v_{C^{(\mathrm{E})}}}{\mathrm{d}t} = \frac{V^{(\mathrm{E})} - v_{C^{(\mathrm{E})}}}{RC^{(\mathrm{E})}} - \frac{i_{L_1^{(\mathrm{E})}} + i_{L_2^{(\mathrm{E})}}}{C^{(\mathrm{E})}} \\ \frac{\mathrm{d}v_{\tilde{C}^{(\mathrm{E})}}}{\mathrm{d}t} = \frac{i_{L_1^{(\mathrm{E})}} - i_{\mathrm{t}}^{(\mathrm{E})}}{\tilde{C}} \\ \frac{\mathrm{d}i_{L_1^{(\mathrm{E})}}}{\mathrm{d}t} = \frac{v_{C^{(\mathrm{E})}} - v_{\tilde{C}^{(\mathrm{E})}}}{L_1} \\ \frac{\mathrm{d}i_{L_2^{(\mathrm{E})}}}{\mathrm{d}t} = \frac{v_{C^{(\mathrm{E})}} - V_{\mathrm{th}}}{L_2} - \frac{k}{L_2}\mathcal{M} \\ \quad \ldots \\ \frac{\mathrm{d}v_{C^{(\mathrm{S}_i)}}}{\mathrm{d}t} = \frac{V^{(\mathrm{S}_i)} - v_{C^{(\mathrm{S}_i)}}}{RC^{(\mathrm{S}_i)}} - \frac{i_{L_1^{(\mathrm{S}_i)}} + i_{L_2^{(\mathrm{S}_i)}}}{C^{(\mathrm{S}_i)}} \\ \frac{\mathrm{d}v_{\tilde{C}^{(\mathrm{S}_i)}}}{\mathrm{d}t} = \frac{i_{L_1^{(\mathrm{S}_i)}} - i_{\mathrm{t}}^{(\mathrm{S}_i)}}{\tilde{C}} \\ \frac{\mathrm{d}i_{L_1^{(\mathrm{S}_i)}}}{\mathrm{d}t} = \frac{v_{C^{(\mathrm{S}_i)}} - v_{\tilde{C}^{(\mathrm{S}_i)}}}{L_1} \\ \frac{\mathrm{d}i_{L_2^{(\mathrm{S}_i)}}}{\mathrm{d}t} = \frac{v_{C^{(\mathrm{S}_i)}} - V_{\mathrm{th}}}{L_2} - \frac{k}{L_2}\mathcal{M} \end{cases} , \qquad (11)$$

where the all-to-all coupling may be conveniently approximated as a mean field having the form

$$\mathcal{M} = \frac{v_{C^{(\mathrm{E})}} + \sum_{i=1}^{n} v_{C^{(\mathrm{S}_i)}}}{n+1} - V_{\mathrm{th}} \, . \qquad (12)$$

This article has been accepted for publication in a future issue of this journal, but has not been fully edited. Content may change prior to final publication. Citation information: DOI 10.1109/ACCESS.2020.2976139, IEEE Access

In a physical setting, the coupling strengths naturally depend on the distances. However, for explanatory purposes, the mean-field representation has the advantage of a compact formulation while retaining a considerable ability to replicate many results obtained in more complex network topologies and processes [49], [50].

Retaining the settings $R = 1500\ \Omega$ and $k = 0.01$, a gradual build-up in the amplitude of the irregular mean-field oscillations was observed, albeit with a nonmonotonic effect: this consisted of a peak $\sigma[\mathcal{M}] \approx 0.1$ V at $V^{(\mathrm{S}_i)} = 1.4$ V, followed by a dip, then a more gradual increase towards $\sigma[\mathcal{M}] \approx 0.12$ V at $V^{(\mathrm{S}_i)} = 5$ V, where $\sigma[x]$ stands for the standard deviation of $x(t)$ (Fig. 6e). Considering the dynamics of the exciter node (E) as a proxy for the state of the entire ensemble of sensors, a pattern similar to the previous scenario was elicited, but with more abrupt transitions. In other words, starting from periodic dynamics, the correlation dimension initially peaked at $D_2^{(\mathrm{E})} \approx 1.9$ for $V^{(\mathrm{S}_i)} = 1.4$ V, then dipped and remained on an elongated plateau at $D_2^{(\mathrm{E})} \approx 1.3$, until $V^{(\mathrm{S}_i)} = 3.6$ V, past which point it rapidly arose towards $D_2^{(\mathrm{E})} \approx 2.8$ (Fig. 6f).

Altogether, these simulations recapitulated the principal phenomena at the basis of the experimental findings discussed next. Very weak inductive coupling appears to be sufficient for engendering moderate or intense levels of phase-locking in these circuits. Moreover, even in the presence of limited entrainment, inductive coupling can cause a transition to chaotic dynamics. Owing to these effects, it is possible, even at relatively large distances for which the coupling coefficient is low, to remotely infer from the dynamics of an exciter node the value of a physical variable at a sensor node, in this case, the applied DC supply voltage. These results straightforwardly extend to a network comprising an ensemble of nodes, among which one can be chosen for signal readout and supplied by a constant voltage, and the others act as sensors. They agree with existing work covering a single pair of coupled Colpitts oscillators, and with a recent analysis of the behavior of diverse numerical and analog electronic systems under situations of weak coupling [31], [51]. By confirming that generative effects are visible even through the lens of highly simplified numerical simulations, the present findings affirm the general validity of the approach well beyond a specific circuit implementation.

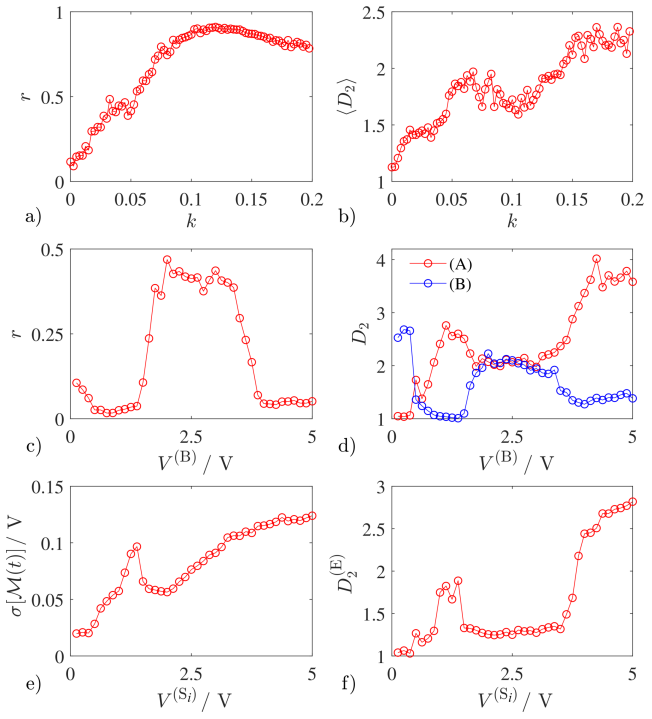

FIGURE 6. Numerical simulation results. a) and b) Effect of the coupling coefficient k on the synchronization r between two oscillators (A)-(B), and the average correlation dimension $\langle D_2 \rangle$ of their dynamics. c) and d) Effect of changing the supply voltage $V^{(\mathrm{B})}$ at one node (B, acting as sensor) while holding it constant at the other (A, acting as exciter). e) and f) Effect of uniformly changing the supply voltage $V^{(\mathrm{S}_i)}$ over an array of $n = 10$ sensor nodes coupled among themselves and to an exciter via a mean field $\mathcal{M}$; $\sigma[\mathcal{M}]$ and $D_2^{(\mathrm{E})}$ denote, respectively, the standard deviation of the mean field and the correlation dimension of the exciter node dynamics.

IV. EXPERIMENTAL OBSERVATIONS AND THEIR INTERPRETATIONS

A. EFFECTS OF INTER-NODE DISTANCE AND SPACING

1) Exciter and one sensor

Ahead of demonstrating the usage of inductively coupled oscillators in measuring a physical variable remotely, it appears necessary to illustrate the synchronization and phase transition phenomena, which can be observed as the coupling strength between network nodes is varied through changing the distances. To this end, as an initial experiment, the effect of coupling between one exciter node (E) and one sensor (S) was investigated, with the latter overlaying the center of the wide-field coil at a distance $d \in [0, 150]$ mm (Fig. 4a). The sensor node was powered by an external DC source $V_{\mathrm{B}} = 5$ V, and its signal was recorded via a probe. Three different configurations A-C were considered, each corresponding to different settings of the DC supply series resistors, namely: $R^{(\mathrm{E})} = 560\ \Omega$, $R^{(\mathrm{S})} = 600\ \Omega$ for A, $R^{(\mathrm{E})} = 760\ \Omega$, $R^{(\mathrm{S})} = 1570\ \Omega$ for B, and $R^{(\mathrm{E})} = 1830\ \Omega$, $R^{(\mathrm{S})} = 350\ \Omega$ for C. The level of phase coherence revealed a marked heterogeneity between these configurations, in that the maximum entrainment was $r \approx 0.2$ for A and B, whereas it was considerably higher for C, namely, $r \approx 0.6$; as expected, in all three cases the synchronization vanished as the nodes were drawn apart (Fig. 7a).

In configuration A, despite the weak synchronization level attained, with decreasing distance the correlation dimension increased across both nodes; namely, from $D_2^{(\mathrm{E})} \approx 1.2$ to $D_2^{(\mathrm{E})} \approx 3.3$ and from $D_2^{(\mathrm{S})} \approx 2.2$ to $D_2^{(\mathrm{S})} \approx 3.8$; albeit with some differences, the permutation entropy followed a similar pattern, in particular via increasing from $h^{(\mathrm{E})} \approx 0.32$ to $h^{(\mathrm{E})} \approx 0.45$ (Fig. 7b). Visual inspection of the spectrogram for the exciter (E) as a function of distance revealed a well-evident and gradual transition to chaos, wherein at long distances, the spectrum was dominated by discrete peaks

This article has been accepted for publication in a future issue of this journal, but has not been fully edited. Content may change prior to final publication. Citation information: DOI 10.1109/ACCESS.2020.2976139, IEEE Access

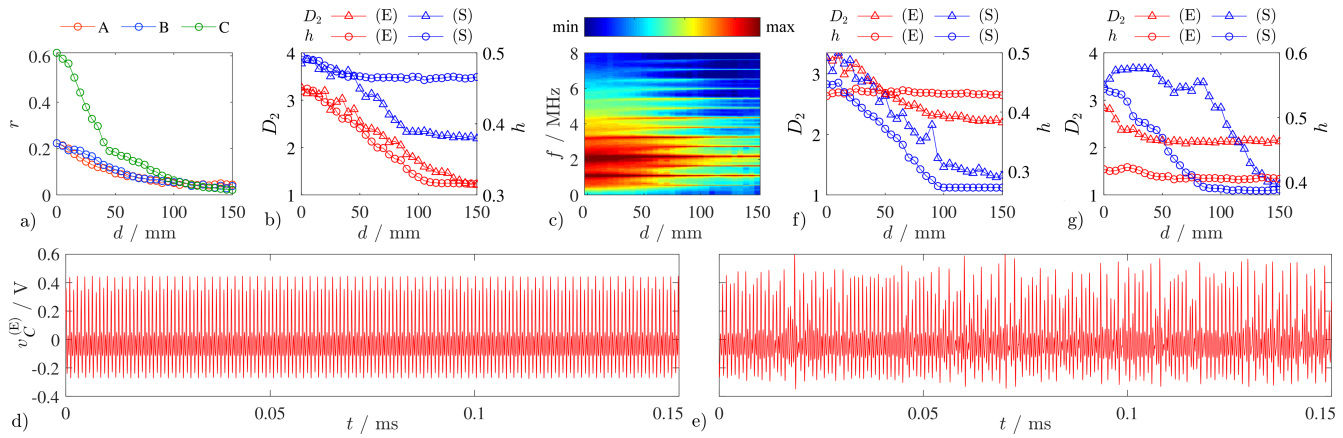

FIGURE 7. Effect of the distance d between the wire-loop coil connected to the exciter node (E) and one sensor board (S) located above it (arrangement in Fig. 4a). a) Synchronization r between the exciter and sensor node for three different configurations A, B and C. b), f) and g) Corresponding correlation dimension D_2 and permutation entropy h. c) Spectrogram for configuration A; color-map reflects the logarithm of the Fourier amplitudes. d) and e) Representative time-series from the exciter node in configuration A, acquired at $d = 150$ mm and $d = 0$ mm, respectively.

at $f \approx \{0.5, 1.1, 1.6, 2.2, 2.7, 3.3, 3.8, 4.3\}$ MHz. As the boards were drawn nearer, the two predominant peaks at $f \approx \{1.1, 2.2\}$ MHz gradually became wider, eventually morphing into a broad distribution over the range 0.3-3.5 MHz and thus hallmarking the transition to chaos (Fig. 7c) [46]. Representative waveforms acquired at the two distance extrema demonstrated the onset of large and low-frequency cycle amplitude fluctuations, in line with previous recordings of oscillators of this kind. Those were, however, rendered chaotic either via control parameter turning or via direct electrical couplings (Fig. 7d,e) [28]–[30], [34].

In configuration B, a different situation was manifest, which exemplified how the effect of coupling strength (distance) may interact with the control parameter settings. On the one hand, the distance had a marked effect on the dynamics of the sensor node (S), with $D_2^{(S)} \approx 1.3$ increasing to $D_2^{(S)} \approx 3.3$ and $h^{(S)} \approx 0.3$ increasing to $h^{(S)} \approx 0.45$. On the other, despite a similar level of synchronization, the effect on the dynamics of the exciter (E) was visibility more constrained, with $D_2^{(E)} \approx 2.2$ increasing to $D_2^{(E)} \approx 3.3$, and $h^{(E)} \approx 0.43$ remaining approximately constant (Fig. 7f). In configuration C, the relative effects on complexity were comparable, albeit at lower levels for the exciter (E); plausibly for the latter reason, an appreciably stronger synchronization ensued, showing the potential decoupling between the two aspects of dynamics (Fig. 7a,g).

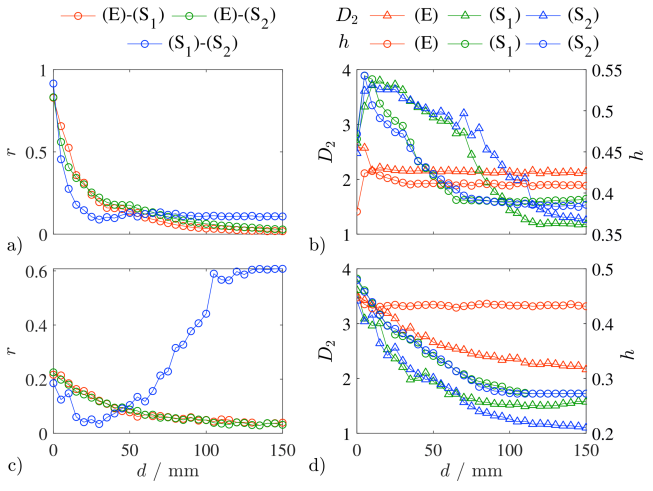

FIGURE 8. Effect of the distance d between the wire-loop coil connected to the exciter node (E) and two co-planar sensor boards (S_1), (S_2) located above it (arrangement in Fig. 4b). a) and c) Synchronization r between the exciter and sensor nodes for two different configurations D and E. b) and d) Corresponding correlation dimension D_2 and permutation entropy h.

2) Exciter and two sensors

Subsequently, to exemplify the simplest scenario of interaction with multiple sensors, the effect of coupling between one exciter node (E) and two sensors (S_1), (S_2) was investigated, with the latter in a coplanar arrangement at a fixed pitch of 75 mm, overlaying the center of the wide-field coil at a distance $d \in [0, 150]$ mm (Fig. 4b). Two different configurations D and E were considered, each corresponding to different settings of the DC supply series resistors, namely: $R^{(E)} = 1830\ \Omega$, $R^{(S_1)} = R^{(S_2)} = 350\ \Omega$ for D, and $R^{(E)} = 760\ \Omega$, $R^{(S_1)} = R^{(S_2)} = 1570\ \Omega$ for E. In configuration D, for distance decreasing below $d \approx 50$ mm, the synchronization between the three nodes raised rapidly, eventually approaching $r \approx 0.9$, which indicates near-perfect phase locking (Fig. 8a). The corresponding effect on the dynamics was visible predominantly for the two sensor nodes, with $D_2^{(S_i)} \approx 1.3$ increasing to $D_2^{(S_i)} \approx 3.6$, whereas the activity of the exciter remained largely insensitive around $D_2^{(E)} \approx 2.2$ (Fig. 8b).

By contrast, in configuration E, for decreasing distance, the synchronization between the exciter (E) and either sensor (S_i) increased gradually up to $r \approx 0.22$, whereas the synchronization between the two sensor nodes themselves, initially $r \approx 0.6$ when far from the exciter coil, dropped

This article has been accepted for publication in a future issue of this journal, but has not been fully edited. Content may change prior to final publication. Citation information: DOI 10.1109/ACCESS.2020.2976139, IEEE Access

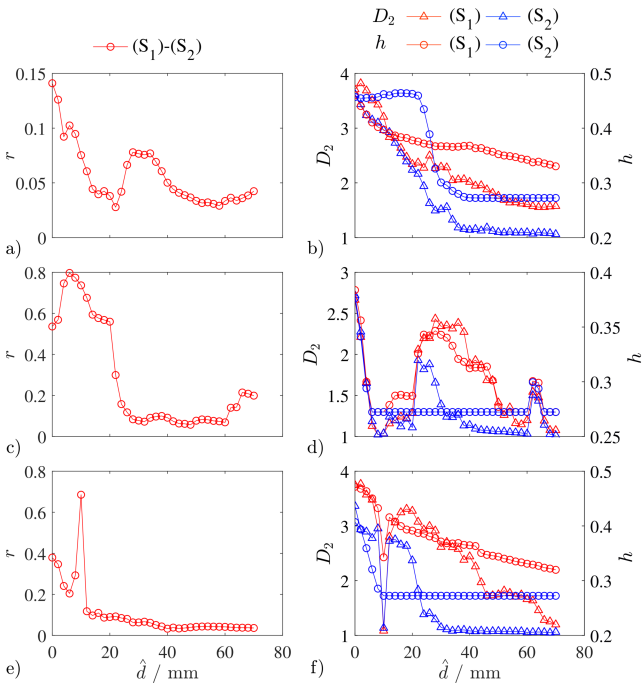

FIGURE 9. Effect of the spacing $\hat{d}$ between two isolate co-planar sensor boards (S_1), (S_2); arrangement in Fig. 4c. a), c) and e) Synchronization r between them for three different configurations F, G and H. b), d) and f) Corresponding correlation dimension D_2 and permutation entropy h.

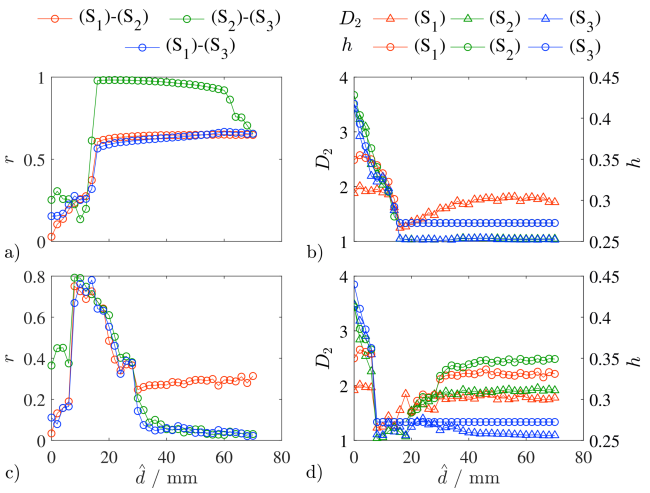

FIGURE 10. Effect of the spacing $\hat{d}$ between two co-planar sensor boards (S_2), (S_3) located next to a third sensor board (S_1); arrangement in Fig. 4d. a) and c) Synchronization r between them for two different configurations I and J. b) and d) Corresponding correlation dimension D_2 and permutation entropy h.

rapidly to the same value (Fig. 8c). This difference illustrated how interaction with the exciter could have both a synchronizing or a desynchronizing effect, depending purely on the control parameter settings; at the same time, the influence on dynamics remained qualitatively similar to the previous case (Fig. 8d).

3) Pair of sensors

Next, to show the phenomena which can arise via interactions between sensor nodes themselves, i.e., away from external perturbation by the exciter, the effect of coupling between two isolated sensors (S_1), (S_2) was investigated, in a coplanar arrangement with a spacing between them $\hat{d} \in [0, 70]$ mm (Fig. 4c). Three different configurations F-H were considered, each corresponding to different settings of the DC supply series resistors, namely: $R^{(S_1)} = 470\ \Omega$, $R^{(S_2)} = 520\ \Omega$ for F, $R^{(S_1)} = 1880\ \Omega$, $R^{(S_2)} = 1840\ \Omega$ for G, and $R^{(S_1)} = 470\ \Omega$, $R^{(S_2)} = 1480\ \Omega$ for H. In configuration F, the synchronization was rather weak, and for decreasing spacing followed a nonmonotonic trend, peaking at $r \approx 0.08$ around $\hat{d} = 30$, then dipping for $\hat{d} = 20$ and increasing towards $r \approx 0.14$ upon direct contact between the boards (Fig. 9a). As the same were drawn nearer, the correlation dimension gradually increased, from $D_2^{(S_i)} \approx \{1.1, 1.6\}$ converging towards $D_2^{(S_i)} \approx 3.6$; the permutation entropy followed a similar trend (Fig. 9b).

In configuration G, the situation was markedly different, in that the synchronization remained relatively low at $r \approx 0.1$ above $\hat{d} = 20$ mm, below which spacing a rapid jump to a considerably higher level $r \approx 0.7$ was observed (Fig. 9c). In this case, the correlation dimension was elevated only for intermediate spacings between $\hat{d} \approx$ 20-50 mm, and mainly for one of the sensors (S_1), further demonstrating the diversified relationship between the dynamical complexity and synchronization (Fig. 9d). In configuration H, yet another pattern was elicited, wherein the synchronization gradually increased up to $r \approx 0.4$. However a sharp peak was observed for $\hat{d} = 10$ mm, at which $r \approx 0.7$, effectively resembling a resonance effect (Fig. 9e). Corresponding to this point, a sharp dip in the correlation dimension values was observed, indicating a transient loss of dynamical complexity; albeit with differences, the effect was visible for both nodes (Fig. 9f). Altogether, these measurements further illustrate the availability of very different influences of the weak coupling upon synchronization in any given configuration, based on the control parameter settings.

4) Chain of sensors

Finally, we illustrate two interaction and relay scenarios which can arise in a chain of three sensor nodes (S_1), (S_2), (S_3), away from external perturbations. There were investigated in a coplanar arrangement with a fixed spacing of 30 mm between the first two, and a variable spacing $\hat{d} \in [0, 70]$ mm between the other two (Fig. 4d); as above, all nodes were powered by an external DC source $V_B = 5$ V and their signals were recorded via probes. Two different configurations I and J were considered, each corresponding to different settings of the DC supply series resistors, namely: $R^{(S_1)} = 1440\ \Omega$, $R^{(S_2)} = 1470\ \Omega$, $R^{(S_3)} = 1330\ \Omega$ for I, and $R^{(S_1)} = 1440\ \Omega$, $R^{(S_2)} = 1070\ \Omega$ and $R^{(S_3)} = 2000\ \Omega$ for J. In configuration I, two regions were clearly identifiable: for $\hat{d} > 20$ mm, near-complete entrainment was present

This article has been accepted for publication in a future issue of this journal, but has not been fully edited. Content may change prior to final publication. Citation information: DOI 10.1109/ACCESS.2020.2976139, IEEE Access

between the nodes (S_2), (S_3) together with a stable moderate entrainment $r \approx 0.6$ between the fixed nodes (S_1), (S_2); below this spacing, the synchronization between all nodes suddenly dropped to $r \approx 0.2$ (Fig. 10a). Consideration of both complexity measures revealed the underlying phenomenon: when the nodes were sufficiently decoupled, their dynamics were largely periodic, whereas drawing the node (S_3) closer caused a collective transition to chaos. Notably, this extended also to node (S_1), thus demonstrating a relay effect by node (S_2) which, through becoming chaotic, also caused it to transition (Fig. 10b).

In configuration J, three situations were apparent: for large spacing $\hat{d} > 30$ mm the entrainment between the nodes (S_2), (S_3) was nearly zero, and accompanied by a moderate level of entrainment $r \approx 0.3$ between the fixed nodes (S_1), (S_2). For small spacings $\hat{d} < 10$ mm, a similar scenario was found, albeit with different relative intensities of synchronization. In between these settings, the nodes reached a high level of collective synchronization, peaking at $r \approx 0.8$ (Fig. 10c). Also in this case, the effect was associated to different levels of complexity: at sufficiently large spacings, it was intermediate $D_2 \approx 1.8$ for the fixed nodes (S_1), (S_2) and low $D_2 \approx 1.1$ for the node (S_3). Accordingly, as the last node (S_3) was drawn nearer, its effect was initially opposite to the previous configuration, in that it drew the other nodes towards periodic dynamics, thus enabling the emergence of synchronization between them. Eventually, however, the couplings became strong enough to cause a collective transition to chaos, with consequent loss of entrainment (Fig. 10d).

5) Relevance and implications

In summary, these experiments demonstrate the remarkable generative potential that, in spite of their simplicity, these oscillators can express when remotely coupled, depending on their topographical layout and on the control parameter settings. Firstly, increasing the coupling strength via reducing the distance can promote a transition to chaos, which may remain localized or engulf the entire network. Secondly, this transition may be accompanied by an elevated synchronization, or occur on its own, even in the absence of significant entrainment. Thirdly, the application of an external field, such as via the wide-field coil of the exciter or a sensor node being drawn nearer, may, depending on the settings, promote the emergence of synchronization or dissipate a synchronization level that preexists. Fourthly, the effect of coupling on synchronization can be highly nontrivial in that, as nodes are drawn near to each other, entrainment may increase gradually, suddenly, or even though a resonance-like peak around a characteristic value. Fifthly, relay effects are readily observed between sensor nodes, for example, arranged as a chain; these may appear in diverse forms, propagating a transition to chaos or transition to periodicity and thus promoting or hindering the diffusion of synchronization at the network level.

Altogether, these phenomena can be accurately understood in terms of the universal properties of nonidentical coupled chaotic oscillators known from existing simulations and experiments. On the one hand, when the control parameters are tuned for operation close to an order-chaos transition, as in the present cases, greater energy exchange generally promotes the onset of chaos due to the absence of an invariant manifold. For the same reason, even at the lowest energy exchange rates, coupling with an oscillator, which is already chaotic, more quickly results in chaos. On the other hand, due to the presence of a limit cycle or an open orbit, the energy exchange rate which is required to maintain a given level of entrainment is considerably lower for periodic than chaotic dynamics [26], [52]–[56].

B. EFFECTS OF SENSED VARIABLE (LUMINOUS FLUX)

1) Isolated sensor

Having established the effects of the interactions between nodes as a function of their topographical arrangement, this section shall demonstrate the ability to perform remote sensing of a physical variable of interest, namely, luminous flux. Initially, we consider the intrinsic dynamics of an isolated sensor node (S), located at a fixed distance of 50 mm underneath a single LED array illuminating it with flux ϕ (Fig. 4e). In all cases considered herein, the sensors were powered purely by their photovoltaic cells, whose output voltage V_B depends on both the luminous flux ϕ and the resistor value R, due to the nonzero equivalent output resistance of the source (Fig. 1b). Given this scenario, it is relevant to evaluate the power requirements of each sensor node: to address this point, given that the current draw i_B could not be measured directly, corresponding values were determined via SPICE simulations based on the `LTspice XVII` environment (Analog Devices, Inc., Norwood MA, USA). Each measured value of V_B was entered, and the corresponding average current $\langle i_B \rangle$ was estimated based on a realistic circuit model.

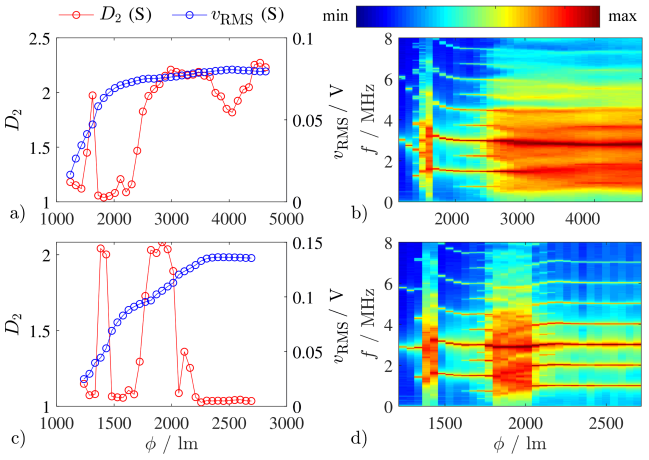

FIGURE 11. Effect of the luminous flux ϕ on an isolated sensor board (S); arrangement in Fig. 4e. a) and c) Correlation dimension D_2 and oscillation amplitude v_{RMS} of the node dynamics for two different configurations K and L. b) and d) Corresponding spectrograms; color-map reflects the logarithm of the Fourier amplitudes.

This article has been accepted for publication in a future issue of this journal, but has not been fully edited. Content may change prior to final publication. Citation information: DOI 10.1109/ACCESS.2020.2976139, IEEE Access

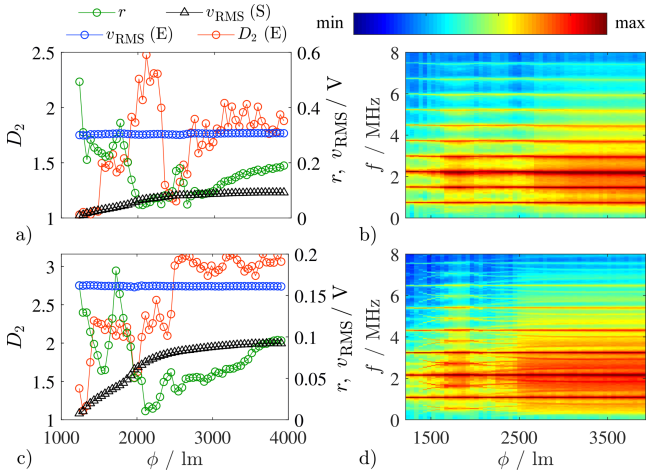

FIGURE 12. Effect of the luminous flux ϕ on a sensor board (S) and exciter node (E), whose wire-loop coil was located at a fixed distance under it (arrangement in Fig. 4f). a) and c) Correlation dimension D_2 of the exciter node dynamics, also oscillation amplitudes v_{RMS} and synchronization r, for two different configurations M and N. b) and d) Corresponding spectrograms (E); color-map reflects the logarithm of the Fourier amplitudes.

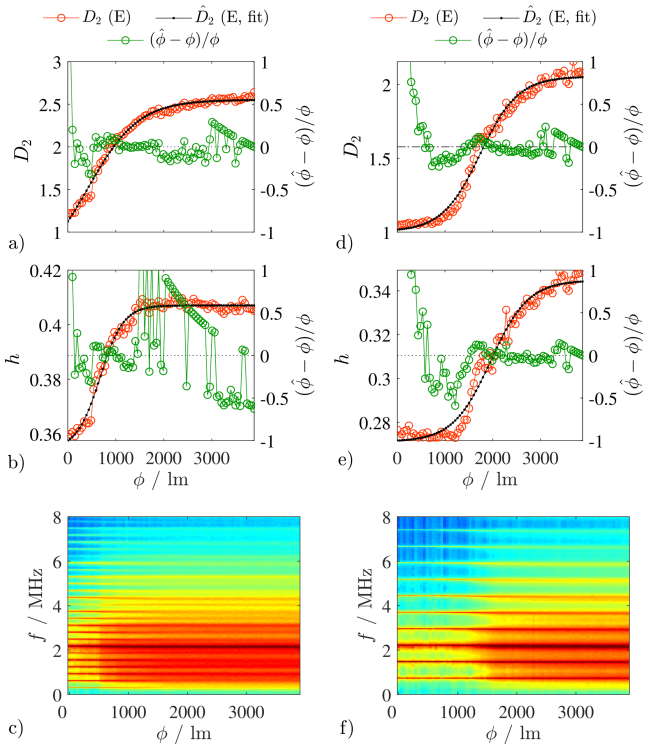

FIGURE 13. Effect of the luminous flux ϕ on a 4×4 array of sensor boards ($\mathrm{S}_{i,j}$) and an exciter node (E), whose wire-loop coil was located at a fixed distance under it (arrangement in Fig. 4g). a) and c) Correlation dimension D_2 of the exciter node dynamics, for two different configurations O and P. b) and d) Corresponding permutation entropy h. For a)-d), sigmoidal fits ($\hat{D}_2$) shown together with the relative error $(\hat{\phi} - \phi)/\phi$ incurred estimating the flux $\hat{\phi}$ from the nonlinear dynamics.

Two different configurations K and L were considered, each corresponding to a setting of the DC supply series resistor, namely: $R^{(\mathrm{S})} = 700\ \Omega$ for K, and $R^{(\mathrm{S})} = 2000\ \Omega$ for L. In configuration K, as the luminous flux was gradually increased, the initially periodic dynamics exhibited a sharp resonance-like transition to chaos for $\phi = 1625$ lm, at which $D_2 \approx 2.0$, followed by a decay back to periodicity $D_2 \approx 1$ up to $\phi = 2300$ lm, beyond which the complexity gradually increased again towards $D_2 \approx 2.2$. The corresponding oscillation amplitude increased gradually with a log-like trend, from $v_{\mathrm{RMS}} \approx 20$ mV up to $v_{\mathrm{RMS}} \approx 80$ mV (Fig. 11a). The corresponding spectrogram as a function of flux revealed a pattern similar to that observed for distance (Fig. 7c), wherein transitions to chaos were associated with a well-evident generation of broad spectral activity over the region 0.3-4.5 MHz (Fig. 11b). Across the first transition to chaos, periodicity dip and subsequent recovery, the supply voltage was recorded as $V_{\mathrm{B}} = \{1.5, 2.1, 3.5\}$ V, with estimated currents $i_{\mathrm{B}} = \{1.1, 1.9, 3.9\}$ mA, corresponding to power draws of $V_{\mathrm{B}} i_{\mathrm{B}} = \{1.7, 4.0, 13.7\}$ mW.

In configuration L, the pattern was different in that the effect of increasing illumination was even more clearly non-monotonic and evident as two distinct chaotic bands between $\phi = 1350$-1450 lm and $\phi = 1750$-2050 lm, wherein $D_2 \approx 2.0$. As in the previous case, the oscillation amplitude v_{RMS} increased gradually (Fig. 11c), and the spectrogram confirmed clear transitions between comb-like and broad spectra corresponding to these regions (Fig. 11d). Across these order-chaos-order-chaos-order transitions, the supply voltage was recorded as $V_{\mathrm{B}} = \{1.9, 2.1, 2.8, 4.5, 5.9\}$ V, with estimated currents $i_{\mathrm{B}} = \{0.6, 0.7, 1.0, 1.9, 2.6\}$ mA, corresponding to power draws of $V_{\mathrm{B}} i_{\mathrm{B}} = \{1.1, 1.5, 2.8, 8.6, 15.3\}$ mW. These initial results confirm the possibility of powering the sensor node photovoltaically, and of rendering its dynamics sensitive to the light intensity, with a relationship determined by the control parameter (series resistor).

2) Exciter and one sensor

Next, we turned to the first proper remote sensing experiment, wherein a similar arrangement as above was prepared, however, with the sensor node (S) coupled to an exciter node (E) located a fixed distance of 50 mm underneath it (Fig. 4f). Two different configurations M and N were considered, each corresponding to different settings of the DC supply series resistors, namely: $R^{(\mathrm{E})} = 1250\ \Omega$, $R^{(\mathrm{S})} = 1900\ \Omega$ for M, and $R^{(\mathrm{E})} = 510\ \Omega$, $R^{(\mathrm{S})} = 1900\ \Omega$ for N. In configuration M, with increasing luminosity the oscillation amplitude gradually grew for the sensor node (S) between $v_{\mathrm{RMS}}^{(\mathrm{E})} \approx$ 10-90 mV while remaining relatively stable $v_{\mathrm{RMS}}^{(\mathrm{E})} \approx 300$ mV for the exciter node (E). The correlation dimension in the dynamics of the latter followed a biphasic trend, starting from $D_2^{(\mathrm{E})} \approx 1$, then peaking at $D_2^{(\mathrm{E})} \approx 2.5$ for $\phi = 2100$ lm, dipping at $D_2^{(\mathrm{E})} \approx 1.2$ for $\phi = 2500$ lm and finally approaching $D_2^{(\mathrm{E})} \approx 1.8$ for $\phi > 2750$ lm (Fig. 12a). As previously observed directly for the sensor node itself, the spectral content closely reflected the level of dynamical complexity, gradually becoming broader with stronger illumination (Fig.

This article has been accepted for publication in a future issue of this journal, but has not been fully edited. Content may change prior to final publication. Citation information: DOI 10.1109/ACCESS.2020.2976139, IEEE Access

12b).

In configuration N, the situation was similar, however, the correlation dimension for the exciter node (E), instead of a biphasic relationship, showed a monotonic step-wise trend, wherein it was initially $D_2^{(\mathrm{E})} \approx 1$, then increased to $D_2^{(\mathrm{E})} \approx 2.3$ and dwelt around this value for $\phi = 1430$-2400 lm, and subsequently increased again towards $D_2^{(\mathrm{E})} \approx 3.0$ (Fig. 12c). The spectral content reflected this trend, in particular, delineating a chaos-chaos transition around $\phi = 2500$ lm (Fig. 12d). These results demonstrate that telemetry based on chaotic oscillators is in principle possible, and, importantly, the relationship between the sensed variable and the dynamics can be modified over qualitatively different function shapes purely based on the local control parameter of the exciter, $R^{(\mathrm{E})}$.

3) Exciter and array of sensors

Subsequently, we considered the case of 4×4 sensors boards ($\mathrm{S}_{i,j}$), laid out in a similar co-planar arrangement at a fixed distance from the exciter node (E) coil. The improve illumination homogeneity, the four LED illuminators were positioned at the corners of the array, providing light incident at a 45° angle; in this experiment, their luminous flux was identically set, i.e., $\phi_{\text{A-D}} = \phi$ (Fig. 4g). Two different configurations O and P were considered, each corresponding to different settings of the DC supply series resistors, namely: $R^{(\mathrm{E})} = 1270\ \Omega$, $R^{(\mathrm{S})} = 970\ \Omega$ for O, and $R^{(\mathrm{E})} = 1270\ \Omega$, $R^{(\mathrm{S})} = 1300\ \Omega$ for P. Here, it should be borne in mind that even though the nominal value of $R^{(\mathrm{S})}$ was identical for all nodes, appreciable parametric mismatches rendered them nonidentical. In each configuration, and separately for the correlation dimension $D_2^{(\mathrm{E})}$ and permutation entropy $h^{(\mathrm{E})}$, the measured relationship between the luminous flux $x = 0.02\phi$ (scaled for instrumental reasons) and the dynamical complexity parameter $y = \{D_2^{(\mathrm{E})}, h^{(\mathrm{E})}\}$ was fit with a sigmoidal function having the form

$$y(x) = \frac{a}{1 + e^{-b(x-c)}} + d\,. \tag{13}$$

A nonlinear least-squares approach was applied, assuming the starting point $a = y(x_{\max}) - y(x_{\min})$, $b = 0.1$, $c = x_{\max}/2$ and $d = y(x_{\min})$, determined based on heuristic criteria. Inverting this function, the flux $\hat{\phi}$ was estimated from the dynamics, and the corresponding relative error $(\hat{\phi} - \phi)/\phi$ was obtained.

In configuration O, the correlation dimension increased gradually from $D_2^{(\mathrm{E})} \approx 1.2$ to $D_2^{(\mathrm{E})} \approx 2.6$, with a larger slope up to $\phi = 2000$ lm. Remarkably, the relationship was nearly perfectly fit assuming the parameter settings $a = 2.1$, $b = 0.09$, $c = 8.5$, $d = 0.47$, yielding $R^2_{\text{adj}} = 0.99$ (variance explained adjusted, not to be confused with resistance); the corresponding median absolute error for $\hat{\phi}$ was 8% (Fig. 13a). The permutation entropy increased nearly linearly up from $h^{(\mathrm{E})} \approx 0.36$ to $h^{(\mathrm{E})} \approx 0.41$ at $\phi = 1400$ lm, with a nearly flat plateau observed thereafter. This relationship was also nearly perfectly fit assuming the parameter settings $a = 0.053$, $b = 0.20$, $c = 13.9$, $d = 0.35$, yielding $R^2_{\text{adj}} = 0.98$; limited to the range $\phi \leq 1400$ lm, the corresponding median absolute error for $\hat{\phi}$ was 11% (Fig. 13b). Accordingly, the spectrogram showed the stronger effect in the range $\phi \leq 1000$ lm, with considerably weaker changes in spectral amplitudes above that level (Fig. 13c).

In configuration P, the increase in correlation dimension was quantitatively more contained, from $D_2^{(\mathrm{E})} \approx 1.0$ to $D_2^{(\mathrm{E})} \approx 2.1$, but more evenly distributed over the span ϕ values. Similarly, it was nearly perfectly fit assuming the parameter settings $a = 1.1$, $b = 0.12$, $c = 35.8$, $d = 1.00$, yielding $R^2_{\text{adj}} = 0.99$; the corresponding median absolute error for $\hat{\phi}$ was also 8% (Fig. 13d). Analogous consideration applied for the permutation entropy, which increased from $h^{(\mathrm{E})} \approx 0.27$ to $h^{(\mathrm{E})} \approx 0.35$, and was nearly perfectly fit assuming the parameter settings $a = 0.074$, $b = 0.12$, $c = 40.3$, $d = 0.27$, yielding $R^2_{\text{adj}} = 0.98$; the corresponding median absolute error for $\hat{\phi}$ was 10% (Fig. 13e). Compared to the previous configuration, the spectrogram showed a more gradual transition to broadband activity, building up around $\phi \approx 1500$ lm (Fig. 13f).

Additional insights into the coupled activity could be obtained by visualizing the attractors reconstructed in two dimensions via time-lag embedding. The dynamics of exciter node (E) delineated a particular snail-like trajectory, which, for low illumination levels, corresponded to a limit cycle, maintaining the same scale but becoming gradually more irregular, hence blurred when averaged over time, with increasing luminous flux on the sensor array (Fig. 14a). On the other hand, due to the increasing supply voltage applied to it, the oscillations of the sensor node (S) steadily grew in amplitude, concomitantly morphing from a circle into a similar snail-like shape (Fig. 14b). Two representative examples of the underlying time-series are visible in Fig. 14c,d.

4) Relevance and implications

Summing up, the results discussed herein unequivocally demonstrated the possibility of performing remote measurements using these oscillators. Firstly, it was possible to power each sensor node via a photovoltaic cell, which also acted as a sensing element because the circuit dynamics were controlled by the supply voltage itself, which depended on the illumination level. Secondly, by coupling two nodes, it was possible to harvest information about the physical variable at the remote node (sensor) from the dynamics of the local one (exciter). Thirdly, when using a single sensor node, even though a relationship between the dynamics and the sensed variable was well evident, this was not univocal and thus problematic to invert.

On the other hand, when multiple sensor nodes were combined, the collective dynamics developed a level of complexity that adequately tracked the parameter to be measured and which was closely reflected in the signal generated by the exciter oscillator. It, therefore, became possible to perform an accurate measurement, which, as more explicitly shown

This article has been accepted for publication in a future issue of this journal, but has not been fully edited. Content may change prior to final publication. Citation information: DOI 10.1109/ACCESS.2020.2976139, IEEE Access

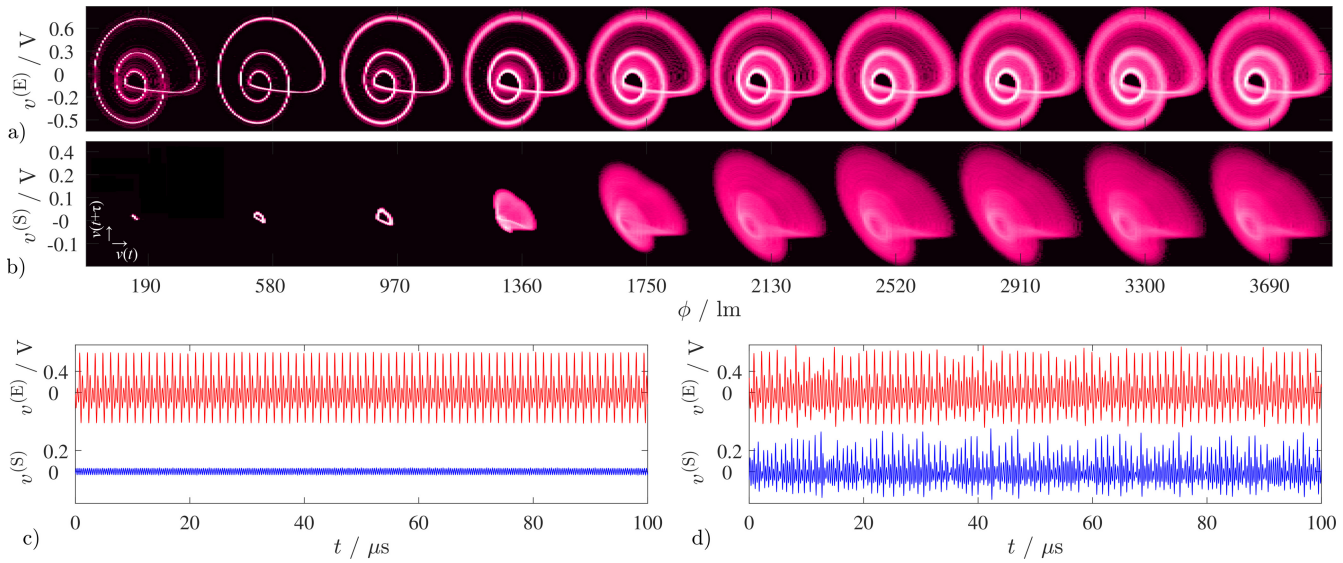

FIGURE 14. Representative examples of the dynamics in a 4×4 array of sensor boards ($S_{i,j}$) and an exciter node (E) as a function of the luminous flux ϕ; phosphorus-like temporal averaging with log-intensity scaling, and same settings as in Fig. 13d-f. a) and b) Two-dimensional time-lag ($\tau = 0.12$ μs) attractor reconstructions for the exciter and the sensor at location (1,1). c) and d) Time-series recorded given flux $\phi = 580$ lm and $\phi = 3300$ lm, respectively.

in the next section, harvested ensemble information from the network as a whole. This offered an issue of calibration, which implied determining a response function and its fitting parameters, as elaborated in other works on distributed and traditional sensing: here, the challenge could be addressed straightforwardly by fitting a sigmoidal curve [57], [58].

C. ADDITIONAL NETWORK MANIPULATIONS

The results reported thus far leave open the question of whether it is the majority of the network contributing to the measured value, or potentially only a subset of influential nodes. Though rigorously addressing this question requires detailed analyses beyond the scope of this work, two additional interventions were performed to gain further insight. Here, we set $R^{(E)} = 525\ \Omega$, $R^{(S)} = 1550\ \Omega$.

1) Incipient damage to sensor array

Firstly, measurements at four representative illumination levels $\phi = \{500, 1500, 2500, 3500\}$ lm were repeated while gradually reducing the number of viable sensor nodes through severing the connection of the respective coupling coils L_2; this operation was iterated until only two oscillators were left active (Fig. 15a). According to the correlation dimension, the parameter distribution observed between these four levels when all $n = 16$ nodes were active, namely $D_2 \approx \{1.4, 2.2, 2.6, 2.8\}$, was only weakly compressed after removing half of the node, yielding $D_2 \approx \{1.3, 2.3, 2.6, 2.6\}$ for $n = 8$. However, when just $n = 2$ oscillators were operating, the distribution was considerably shrunk towards low values, even though the rank positions were preserved, with $D_2 \approx \{1.2, 1.6, 1.8, 1.9\}$ (Fig. 15b). The permutation entropy revealed an analogous pattern, albeit with a considerably more marked effect of the number of active nodes: for $n = 16$, $h \approx \{0.38, 0.39, 0.41, 0.42\}$, but already for $n = 8$, this range was significantly compressed towards lower values, into $h \approx \{0.38, 0.39, 0.40, 0.40\}$; for $n \leq 6$, the rank positions were lost (Fig. 15c).

2) Incomplete illumination

Secondly, measurements sweeping the luminous flux emitted by each LED over $\phi \in [0, 3900]$ lm were repeated while illuminating only $m = 1, 2, 3, 4$ quadrants (i.e., 25%, 50%, 75% and 100% of the array area), and averaging over all possible combinations for each value of m (i.e., zones A-D in Fig. 15d). The correlation dimension, which gradually increased with stronger illumination, was visibly higher depending on the number of illuminated quadrants, for all settings $\phi > 1500$ lm; the relationship was, however, clearly sub-linear. For example, at $\phi = 2000$ lm the correlation dimension was $D_2 \approx \{2.1, 2.3, 2.5, 2.6\}$; however, at $\phi = 3900$ lm, it was $D_2 \approx \{2.4, 2.6, 2.7, 2.9\}$. In other words, even though the rank positions were consistent, between one and four illuminated quadrants D_2 increased only by $\approx 20\%$ (Fig. 15e). The situation was analogous for the permutation entropy, with $h \approx \{0.38, 0.39, 0.40, 0.41\}$ for $\phi = 2000$ lm and $h \approx \{0.39, 0.40, 0.41, 0.42\}$ for $\phi = 3900$ lm (Fig. 15f).

3) Relevance and implications

These results confirm that the collective dynamics reflect an ensemble evaluation over a representative multitude of nodes. On the one hand, the number of electrically viable or illuminated sensors had an evident influence on the measurement, rendering it sufficiently indicative of a sum or average operation, which represents the predominant requirement in distributed sensing [10]–[14]. On the other, albeit with some differences between the correlation dimension and permuta-

This article has been accepted for publication in a future issue of this journal, but has not been fully edited. Content may change prior to final publication. Citation information: DOI 10.1109/ACCESS.2020.2976139, IEEE Access

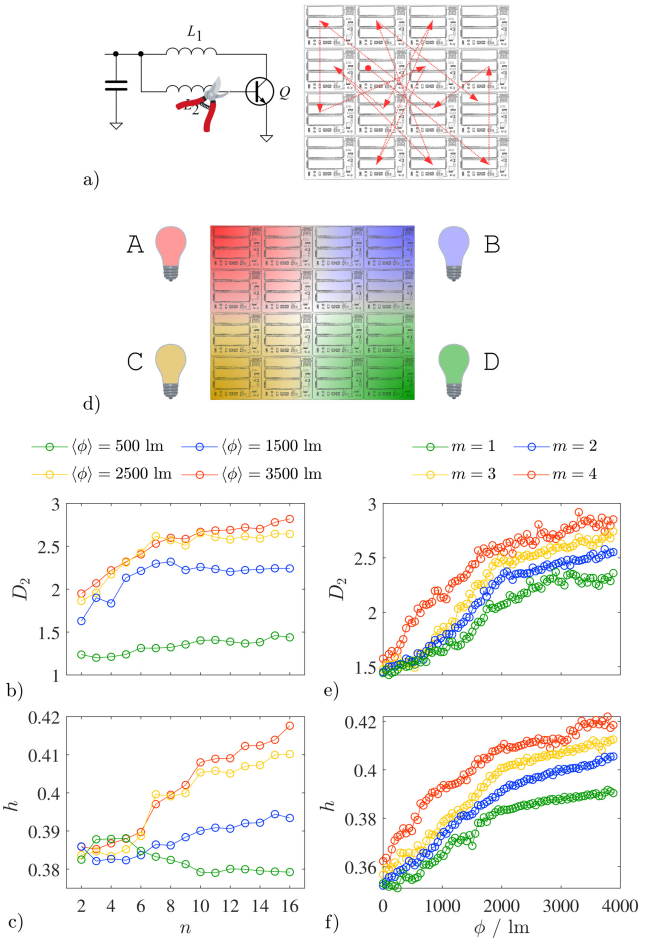

FIGURE 15. Additional interventions on a 4×4 array of sensor boards ($S_{i,j}$) and an exciter node (E), whose wire-loop coil is located at a fixed distance under it (arrangement in Fig. 4g). a) Gradually reducing the number of viable sensors n in a pseudo-random sequence via severing the coupling coils. b) and c) Corresponding correlation dimension D_2 and permutation entropy h curves. d) Partial illumination of only m quadrants (averaged over all combinations of the zones A-D). e) and f) Corresponding correlation dimension D_2 and permutation entropy h curves.

tion entropy, the relationship between the illumination level and the dynamics was relatively resilient to the loss of a subpopulation of nodes, remaining well visible even when only half of the network was retained. These two features are of central importance to distributed sensing since its purpose is obtaining a robust ensemble measurement that is not excessively influenced by a minority of sensors, while at the same time ensuring that viability is maintained up to a moderate level of damage, which in real-life scenarios could ensue due to spontaneous failure or deliberate attack [7], [10], [11], [59], [60].

The sublinear relationship elicited for the sensed variable, as well as the number of sensors, is inherent in the nature of the system, which is governed by synergistic rather than summative interactions (as would be, for instance, in the case of pure transmitters whose output power gets integrated spatially). While a transition from periodicity to chaos can be engendered relatively straightforwardly in the presence of sufficient nonlinearity, and the chaotic dynamics can be enriched via couplings, the dimensionality is eventually bound by the finiteness of the system. Approaching dimensional saturation (that is, attaining a strange attractor whose fractional dimension nears the number of physical variables in the phase space) may be hindered by the weak level of couplings [26], [30]. A clear demonstration of this phenomenon for experimental and simulated systems can be found, for example, in a recent study of star networks but also in realizations of the present single-transistor oscillator with fractal elements [34], [51]. Finally, the negative bias of the complexity estimators should be borne in mind, potentially accounting for the steeper slopes observed for the permutation entropy than the correlation dimension [42]–[45].

V. CONCLUSIONS AND FUTURE APPLICATIONS

A. CONTRIBUTION

This precursory study aimed to bring together two research fields that, thus far, had remained mostly separate: wireless sensor networks and electronic chaotic oscillators. It demonstrated that it is, in principle, possible to realize a viable distributed sensing system while implementing each node with a simple analog circuit, consisting only of a single transistor and a limited number of passive components, rather than a microprocessor-based entity. In other words, the explicitly-coded behavior of an automaton is replaced by the nonlinear dynamics of an oscillator, fuzzy and heterogeneous, powerfully capable of giving rise to complex emergent phenomena via synchronization [61]–[63].

Because the present approach is new, there is limited literature to which direct comparisons can be made. In this regard, the most important study is that in Ref. [31]: therein, the experimental synchronization of two inductively-coupled Colpitts oscillators was demonstrated. Synchronization and chaotic transitions were demonstrated as a function of the coupling coefficient k. However, no usage in remote sensing was elaborated, and only one configuration was considered, namely an oscillator pair, as opposed to the seven arrangements of sensor and exciter nodes considered herein; moreover, the transistor circuit was structurally more complex. At a more general level, the present results are well in line with existing work on the synchronization of chaotic oscillators using direct electrical connections [27], [28], [51].

Even though for demonstration purposes in this work the oscillators were realized using discrete components and had a current draw on the order of milliwatts, it is well established that, on a mainstream CMOS process node, single-chip chaos generators can be implemented with an area and power footprint on the order of ≈ 0.03 mm^2 and ≈ 0.05 μW. A distributed sensing approach hinged around simple oscillators, therefore, appears ideally suited for the realization of fine-granularity smart dust sensors, insofar as future work can realize on-chip, via appropriate feature size and frequency scaling (e.g., X band and beyond), both the coupling antenna and an energy harvesting system (electro-

This article has been accepted for publication in a future issue of this journal, but has not been fully edited. Content may change prior to final publication. Citation information: DOI 10.1109/ACCESS.2020.2976139, IEEE Access

magnetic, electromechanical, thermoelectric or photovoltaic) [10], [64]–[68].

B. NOVELTY

To the authors' knowledge, these findings represent the first physical demonstration that chaotic oscillators may be coupled remotely in an extended network, expanding previous work limited to an isolated node pair [31]. A particularly relevant result, which is expected to have general validity, is that emergent phenomena such as synchronization, desynchronization, relaying, and chaotic transitions could be elicited, as a function of both the network topography and the sensed physical variable, even in the presence of weak coupling. Importantly, the coupling coefficients under consideration, on the order of ≈ 0.01, are expected to be unproblematic to realize over considerably longer distances, on the order of meters and beyond, using optimized electromagnetic structures. It should be noted that even this though initial laboratory demonstration was based on simple inductive coupling, without any attempt at design optimization, the mechanisms are expected to straightforwardly generalize to diverse antenna types, as well as to frequencies well-suited for on-chip coil realization [36], [64], [67].

A specific aspect of novelty is the readout of the network dynamics via an active exciter node coupled to all sensors, that is, a structurally identical oscillator possessing its intrinsic dynamics. Due to the bidirectional nature of the inductive coupling, the dynamics of this node may both be influenced by and act upon the dynamics of the remote sensor nodes, which is unlike the simple averaging performed by a passive receiver. As exemplified by the configurations considered, this allowed realizing different interaction patterns, such as the transition to synchronization or chaotic state, only as a function of the local control parameter (series resistor value) within the exciter node (which would, in an application, functionally correspond to a base-station). Furthermore, depending on the settings, it enabled the externally-applied excitation field to enhance or hinder synchronization among the sensors. Sensing via applying an external excitation is pervasive across physical measurement techniques, most notably nuclear magnetic resonance, and rhymes with the notion of harvesting information about a complex network via externally perturbing it; however, this approach had seemingly not yet been applied to wireless sensor networks [69]–[71]. Future work should investigate it more extensively, elucidating its advantages over a passive receiver also in terms of sensitivity and selectivity, and considering more advanced configurations such as a possibly adaptive exciter node capable of rapidly sweeping its control parameter.

C. APPLICATIONS

For demonstration purposes, here, the sensed variable, namely the light intensity, coincided with the power source for the sensor nodes. The approach, however, is entirely generic and may be realized with other configurations, and other nonlinear electronic oscillators; for example, a sensing element could be instanced corresponding to the supply resistor, or the tank capacitor, while the node is powered at a voltage unrelated to the sensed variable. Indeed, previous work has demonstrated that the dynamics of these circuits are more responsive to the series resistance than to the supply voltage [28], [30].

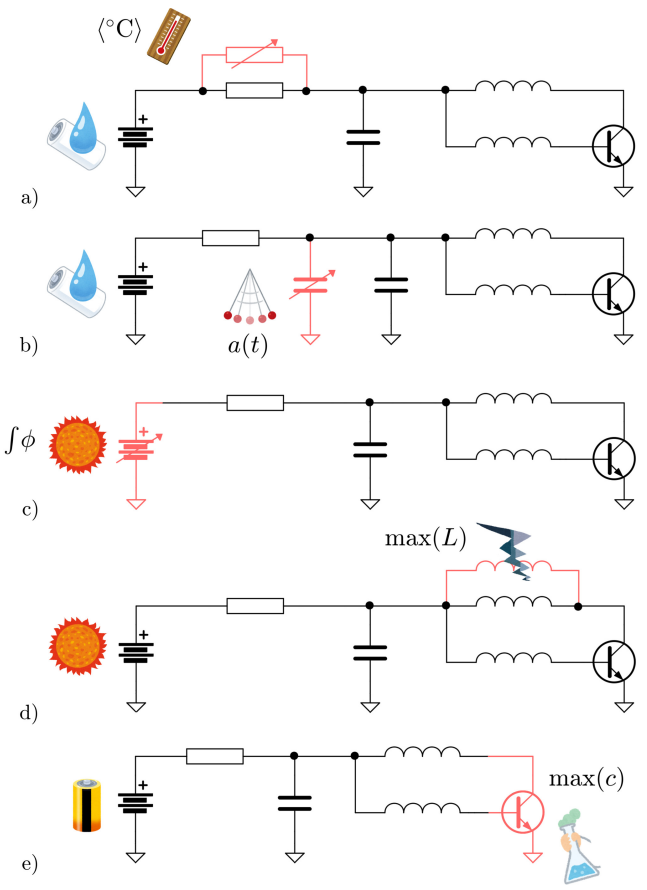

FIGURE 16. Examples of possible future application concepts. a) Monitoring of average human body temperature $\langle°\mathrm{C}\rangle$, via a resistive temperature sensor and a biological electrochemical power source (e.g., sweat). b) Monitoring of human oscillatory movement $a(t)$ (e.g., tremor), with oscillator synchronization via a capacitive acceleration sensor. c) Monitoring of total solar photon flux density $\int \phi$ in an agricultural field, via a photovoltaic cell acting both as sensor and power source. d) Monitoring of cracking in a concrete structure, via a break wire inductor (maximum inductance $\max(L)$) and a photovoltaic power source. e) Monitoring of the concentration $\max(c)$ of an analyte via a chemically-sensitive transistor and long-life battery. Coupling infrastructure not shown, sensorized circuit element highlighted in red.

The concrete next steps towards prototype implementations shall depend on the specific application scenarios. For example, in a biomedical scenario, low-energy oscillators could be powered by an electrochemical source based on sweat, and the body itself could act as an electrical coupling medium between the oscillators. The accurate approximation of core body temperature from noninvasive measurements is knowingly challenging, hence application of the present techniques to obtain a large-area average could be beneficial [6], [72]; this could be realized by altering the series supply

resistor via a suitably-sized parallel thermistor (Fig. 16a). Insofar as the oscillation frequency (or a secondary, modulating component) can be lowered down to the range of ≈ 5 Hz to allow direct synchronization between the physiological and electronic dynamics, coupled oscillators could also find applications in the detection of subclinical tremors in movement disorders. One approach may be coherently integrating them over multiple limb locations, for instance through capacitive micro-sensors (Fig. 16b); a similar method could also be applied to monitoring the oscillation of an engineered structure [73], [74].

In an agricultural scenario, the present demonstration of average illumination estimation could have immediate relevance to the determination of the solar photon flux density, provided that the coupling coils are redesigned and scaled to operate on the range of at least several meters (Fig. 16c). Towards such an application, via the relay mechanisms demonstrated in the present results, it could be helpful to exploit a small subset of nodes as a proxy for the state of the entire network [4]. Differently, in a civil engineering scenario, one could envisage a network of these oscillators being coupled via a conductive structural element and individually equipped with a wire break sensor altering, for example, the value of one of the coils when opened [75], [76]. The nodes could be tuned for collective oscillation close to chaos transition in such a manner that, rather than representing an ensemble average, the dynamics suddenly turn chaotic if one sensor is damaged, triggering an alarm (Fig. 16d). Further, in suitable chemical sensing applications, even the transistor itself could act as a sensing element for the concentration of an analyte (Fig. 16e) [77].

Lastly, diverse forms of coupled nonlinear networks can provide viable substrates for physical reservoir computing. Therefore, insofar as the nodes are distributed sufficiently densely to ensure the emergence of collective behavior, the paradigm of remote chaotic synchronization could be used as a basis to implement distributed forms of reservoir computing over wireless sensor networks [78], [79]. At the same time, the elementary nature of single-transistor oscillators renders them ideally suited for realization in the form of flexible and printed electronics, considerably expanding the pervasiveness of the distributed sensor nodes that can be realized vastly beyond what is presently possible, one example being skin patch transducers [80], [81].

ACKNOWLEDGEMENT

L. Minati gratefully acknowledges employment and research funding by the World Research Hub Initiative (WRHI), Institute of Innovative Research (IIR), Tokyo Institute of Technology, Tokyo, Japan. This work was partly supported by JSPS KAKENHI Grant Numbers 16H02337 and 19H02191.

REFERENCES

[1] L.A. Schintler, S.P. Gorman, A. Reggiani, R. Patuelli, A. Gillespie, P. Nijkamp, and J. Rutherford, "Complex Network Phenomena in Telecommunication Systems," Netw Spat Econ., vol. 5, no. 4, pp. 351–370, Dec. 2005.

[2] Y.-Y.Liu, and A.-L. Barabási, "Control principles of complex systems," Rev. Mod. Phys., vol. 88, pp. 035006, Sep. 2016.

[3] K. Batool, and M.A. Niazi, "Modeling the internet of things: a hybrid modeling approach using complex networks and agent-based models," zi Complex. Adapt. Syst. Model., vol. 5, no. 1, pp. 1–19, Dec. 2017.

[4] T. Ojha, S. Misra, and N.S. Raghuwanshi, "Wireless sensor networks for agriculture: The state-of-the-art in practice and future challenges," Comput. Electron. Agr., vol. 118, pp. 66-84, Sep. 2015.

[5] D.M. Broday, and The Citi-Sense Project Collaborators, "Wireless Distributed Environmental Sensor Networks for Air Pollution Measurement—The Promise and the Current Reality," Sensors, vol. 17, no. 10, pp. 2263, Oct. 2017.

[6] R.A. Khan, and A.-S.K. Pathan, "The state-of-the-art wireless body area sensor networks: A survey", Int. J. Sens. Netw., doi: 10.1177/1550147718768994, Apr. 2018.

[7] F. Mao, K. Khamis, S. Krause, J. Clark, and D.M. Hannah, "Low-Cost Environmental Sensor Networks: Recent Advances and Future Directions," Front. Earth Sci., vol. 7, pp. 221, Sep. 2019.

[8] A. Ukil, H. Braendle and P. Krippner, "Distributed Temperature Sensing: Review of Technology and Applications," IEEE Sens. J., vol. 12, no. 5, pp. 885-892, May. 2012.

[9] X. Lu, P.J. Thomas, and J.O. Hellevang, "A Review of Methods for Fibre-Optic Distributed Chemical Sensing," Sensors, vol. 19, no. 13, pp. 2876, Jun. 2019.

[10] J.M. Kahn, R.H. Katz, and K.S.J. Pister, "Emerging challenges: Mobile networking for "Smart Dust"," J. Commun. Netw., vol. 2, no. 3, pp. 188-196, Sep. 2000.

[11] D. Puccinelli, and M. Haenggi, "Wireless sensor networks: applications and challenges of ubiquitous sensing," IEEE Circuits Syst. Mag., vol. 5, no. 3, pp. 19-31, 2005.

[12] C. Guyeux, M. Haddad, M. Hakem, M. Lagacherie, "Efficient distributed average consensus in wireless sensor networks," Comput. Commun., vol. 150, pp. 115-121, Jan. 2020.

[13] M. Wang, J. Cao, B. Chen, Y. Xu, and J. Li, "Distributed Processing in Wireless Sensor Networks for Structural Health Monitoring," in J. Indulska, J. Ma, L.T. Yang, T. Ungerer, and J. Cao (Eds.), Distributed Processing in Wireless Sensor Networks for Structural Health Monitoring, pp. 103-112, Springer Berlin Heidelberg, 2007.

[14] A. Khosravi, and Y.S. Kavian, "Challenging issues of average consensus algorithms in wireless sensor networks," IET Wirel. Sens. Syst., vol. 6, no. 3, pp. 60-66, Jul. 2016.

[15] J.M.T. Portocarrero, F.C. Delicato, P.F. Pires, N. Gámez, L. Fuentes, D. Ludovino, and P. Ferreira, "Autonomic Wireless Sensor Networks: A Systematic Literature Review," J. Sens., pp. 782789, Dec. 2014.

[16] H. Leung, S. Chandana and S. Wei, "Distributed sensing based on intelligent sensor networks," IEEE Circ. Syst. Mag., vol. 8, no. 2, pp. 38–52, May. 2008.

[17] F. Sivrikaya, and B. Yener, "Time synchronization in sensor networks: a survey," IEEE Network, vol. 18, no. 4, pp. 45-50, Jul-Aug. 2004.

[18] K. Konishi, and H. Kokame, "Synchronization of pulse-coupled oscillators with a refractory period and frequency distribution for a wireless sensor network," Chaos, vol. 18, pp. 033132, Sep. 2008.

[19] C.C. Canavier, and S. Achuthan, "Pulse coupled oscillators and the phase resetting curve," Math. Biosci., vol. 226, pp. 77-96, May. 2010.

[20] T. Okuda, K. Konishi, and N. Hara, "Experimental verification of synchronization in pulse-coupled oscillators with a refractory period and frequency distribution," Chaos, vol. 21, pp. 023105, Sep. 2011.

[21] M.J. Ogorzalek, Z. Galias, A.M. Dabrowski and W.R. Dabrowski, "Chaotic waves and spatio-temporal patterns in large arrays of doubly-coupled Chua's circuits," IEEE Trans. Circuits Syst., vol. 42, no. 10, pp. 706-714, Oct. 1995.

[22] A. Pikovsky, M. Rosenblum, and J. Kurths, *Synchronization: A Universal Concept in Nonlinear Sciences*, Cambridge University Press, Cambridge UK (2003).

[23] A. Bergner, M. Frasca, G. Sciuto, A. Buscarino, E.J. Ngamga, L. Fortuna, and J. Kurths, "Remote synchronization in star networks," Phys. Rev. E, vol. 85, no. 2, pp. 026208, Feb. 2012.

[24] L.M. Pecora, F. Sorrentino, A.M. Hagerstrom, T.E. Murphy, and R. Roy, "Cluster synchronization and isolated desynchronization in complex networks with symmetries," Nat. Commun., vol. 5, pp. 4079, Jun. 2014.

[25] Y. Wang, L. Wang, H. Fan, and X. Wang, "Cluster synchronization in networked nonidentical chaotic oscillators," Chaos, vol. 29, pp. 093118, Aug. 2019.

[26] S. Boccaletti, J. Kurths, G. Osipov, D.L. Valladares, and C.S. Zhou, "The synchronization of chaotic systems," Phys. Rep., vol. 366, no. 1-2, pp. 1–101, Aug. 2002.

[27] L. Fortuna, and M. Frasca, "Experimental synchronization of single-transistor-based chaotic circuits," Chaos, vol. 17, pp. 043118, Oct. 2007.

[28] L. Minati, "Experimental synchronization of chaos in a large ring of mutually coupled single-transistor oscillators: Phase, amplitude, and clustering effects," Chaos, vol. 24, pp. 043108, Sep. 2014.

[29] L. Minati, "Experimental dynamical characterization of five autonomous chaotic oscillators with tunable series resistance," Chaos, vol. 24, p. 033110, Jul. 2014.

[30] L. Minati, M. Frasca, P. Oświęcimka, L. Faes, and S. Drożdż, "Atypical transistor-based chaotic oscillators: Design, realization, and diversity," Chaos, vol. 27, no. 7, pp. 073113, Jul. 2017.

[31] L.K. Kana, A. Fomethe, H.B. Fotsin, E.T. Wembe, and A.I. Moukengue, "Complex Dynamics and Synchronization in a System of Magnetically Coupled Colpitts Oscillators," J. Nonlinear Dyn., pp. 5483956, Apr. 2017.

[32] P. Canyelles-Pericas, P.A. Haigh, Z. Ghassemlooy, A. Burton, X. Dai, T. The Son, H. Le-Minh, R. Binns, and K. Busawon, "Chaos Synchronization in Visible Light Communications with Variable Delays Induced by Multipath Fading," Appl. Syst. Innov., vol. 1, pp. 45, Nov. 2018.

[33] M. Pontón, and A. Suárez, "Stability analysis of wireless coupled-oscillator circuits," 2017 IEEE MTT-S International Microwave Symposium (IMS), Honololu, HI, 2017, pp. 83-86.

[34] L. Minati, M. Frasca, G. Giustolisi, P. Oświęcimka, S. Drożdż, and L. Ricci, "High-dimensional dynamics in a single-transistor oscillator containing Feynman-Sierpiński resonators: Effect of fractal depth and irregularity," Chaos, vol. 28, no. 9, pp. 093112, Sep. 2018.

[35] Publicly Available Data, accessed on Dec. 19, 2019. [Online]. Available: http://www.lminati.it/listing/2020/a/.

[36] E. Guthrie, A. Frolenkov, and J.O. Mur-Miranda, "Limit behavior of the magnetic coupling coefficient for mid-range, near-field applications," J. Phys. Conf., vol. 476, pp. 012116, Dec. 2013.

[37] F. Takens, "Detecting Strange Attractors in Turbulence," Lecture Notes in Math., vol. 898, pp. 366–381, Springer, New York (1981).

[38] A.M. Fraser, and H.L. Swinney, "Independent coordinates for strange attractors from mutual information," Phys. Rev. A, vol. 33, no. 2, pp. 1134–1140, Feb. 1986.

[39] T. Sauer, J.A. Yorke, and M. Casdagli, "Embedology," J. Stat. Phys., vol. 65, no. 3, pp. 579–616, Nov. 1991.

[40] A. Provenzale, L.A. Smith, R. Vio, and G. Murante, "Distinguishing between low-dimensional dynamics and randomness in measured time series," Physica D, vol. 58, no. 1-4, pp. 31–49, Sep. 1992.

[41] R. Hegger, H. Kantz and T. Schreiber, "Practical implementation of nonlinear time series methods: The TISEAN package," Chaos, vol. 9, pp. 413, May 1999.

[42] P. Grassberger, and I. Procaccia, "Measuring the strangeness of strange attractors," Physica D, vol. 9, no. 1, pp. 189-208, Oct. 1983.

[43] K. P. Michalak, "How to estimate the correlation dimension of high-dimensional signals?," Chaos, vol. 24, no. 3, pp. 033118, Jul. 2014.

[44] C. Bandt, and B. Pompe, "Permutation entropy: A natural complexity measure for time series," Phys Rev Lett., vol. 88, no. 17, p. 174102, Apr. 2002.

[45] M. Riedl, A. Muüller, and N. Wessel, "Practical considerations of permutation entropy," Eur Phys J Spec Top., vol. 222, no. 2, pp. 249–262, Jun. 2013.

[46] E. Ott, Chaos in Dynamical Systems., Cambridge University Press, Cambridge UK (2002).

[47] J. Millman and A. Grabel, Microelectronics, McGraw-Hill, New York, 1987.

[48] L.F. Shampine, and M.W. Reichelt, "The MATLAB ODE Suite," SIAM J. Sci. Comput., vol. 18, no. 1, pp. 1–22, 1997.

[49] L.P. Kadanoff, "More is the Same; Phase Transitions and Mean Field Theories," J. Stat. Phys., vol. 137, no. 5, pp. 777-797, Sep. 2009.

[50] J.P. Gleeson, S.Melnik, J.A. Ward, M.A. Porter, and P.J. Mucha, "Accuracy of mean-field theory for dynamics on real-world networks," Phys. Rev. E, vol. 85, no. 2, pp. 026106, Feb. 2012.

[51] L. Minati, H. Ito, A. Perinelli, L. Ricci, L. Faes, N. Yoshimura, Y. Koike, and M. Frasca, "Connectivity Influences on Nonlinear Dynamics in Weakly-Synchronized Networks: Insights From Rössler Systems, Electronic Chaotic Oscillators, Model and Biological Neurons," IEEE Access, vol. 7, pp. 174793-174821, Dec. 2019.

[52] M.G. Rosenblum, A.S. Pikovsky, and J. Kurths, "Phase Synchronization of Chaotic Oscillators," Phys. Rev. Lett., vol. 76, no. 11, pp. 1804-1807, Mar. 1996.

[53] G.V. Osipov, A.S. Pikovsky, M.G. Rosenblum, and J. Kurths, "Phase synchronization effects in a lattice of nonidentical Rössler oscillators," Phys. Rev. E, vol. 55, no. 3, pp. 2353-2361, Mar. 1997.

[54] E. Rosa, E. Ott, and M.H. Hess, "Transition to Phase Synchronization of Chaos", Phys. Rev. Lett., vol. 80, no. 8, pp. 1642-1645, Feb. 1998.

[55] I.A. Heisler, T. Braun, Y. Zhang, G. Hu, and H.A. Cerdeira, "Experimental investigation of partial synchronization in coupled chaotic oscillators," Chaos, vol. 13, no. 1, pp. 185-194, Feb. 2003.

[56] A. Baziliauskas, R. Krivickas, and A. Tamaševičius, "Coupled Chaotic Colpitts Oscillators: Identical and Mismatched Cases," Nonlinear Dyn., vol. 44, no. 1, pp. 151-158, Jun. 2006.

[57] T. Fujino, and S. Honda, "Automatic Calibration of Sensing Systems for Distributed Physical Fields," SICE J. Contr. Meas. Syst. Int., vol. 6, no. 3, pp. 221-229, May. 2013.

[58] T. Islam, and S.C. Mukhopadhyay, "Linearization of the sensors characteristics: a review," Int. J. Smart Sens. Intel. Syst., vol. 12, no. 1, pp. 1-21, Aug. 2019.

[59] Y. Chen, S. Kar and J.M.F. Moura, "Resilient Distributed Estimation: Sensor Attacks," , IEEE Trans. Autom. Control., vol. 64, no. 9, pp. 3772-3779, Sep. 2019.

[60] Y. Huang, J.F. Martínez, J. Sendra, and L. López, "Resilient Wireless Sensor Networks Using Topology Control: A Review," Sensors, vol. 15, no. 10, pp. 24735-24770, Sep. 2015.

[61] K.P. O'Keeffe, H. Hong, and S.H. Strogatz, "Oscillators that sync and swarm," Nat. Commun., vol. 8, pp. 1504, Nov. 2017.

[62] L. Minati, "Across Neurons and Silicon: Some Experiments Regarding the Pervasiveness of Nonlinear Phenomena," Acta Phys Pol B, vol. 49, pp. 2029, Dec. 2018.

[63] S. Boccaletti *et al.*, *Synchronization: From Coupled Systems to Complex Networks*, Cambridge University Press, Cambridge UK (2018).

[64] H. Gao, M.K. Matters-Kammerer, P. Harpe, D. Milosevic, A. van Roermund, J.-P. Linnartz, and P.G.M. Baltus, "A 60-GHz energy harvesting module with on-chip antenna and switch for co-integration with ULP radios in 65-nm CMOS with fully wireless mm-wave power transfer measurement," 2014 IEEE International Symposium on Circuits and Systems (ISCAS), Melbourne VIC, 1-5 June 2014, pp. 1640-1643.

[65] D. Li, S. Ogrenci-Memik and L. Henschen, "On-chip integration of thermoelectric energy harvesting in 3D ICs," 2015 IEEE International Symposium on Circuits and Systems (ISCAS), Lisbon, 24-27 May 2015, pp. 1078-1081.

[66] I. Cevik, X. Huang, H. Yu, M. Yan, and S.U. Ay SU, "An ultra-low power CMOS image sensor with on-chip energy harvesting and power management capability," Sensors, vol. 15, no. 3, pp. 5531-54, Mar. 2015.

[67] S. Mandal, S.K. Mandal, and A.K. Mal, "On-chip antennas using standard CMOS technology: A brief overview," 2017 International Conference on Innovations in Electronics, Signal Processing and Communication (IESC), Shillong, 6-7 Apr. 2017, pp. 74-78.

[68] L. Minati, M. Frasca, N. Yoshimura, L. Ricci L, P. Oświęcimka, Y. Koike, K. Masu, and H. Ito, "Current-Starved Cross-Coupled CMOS Inverter Rings as Versatile Generators of Chaotic and Neural-Like Dynamics Over Multiple Frequency Decades," IEEE Access, vol. 7, pp. 54638-54657, Apr. 2019.

[69] M.E. Smith, and J.H. Strange, "NMR techniques in materials physics: a review," Meas. Sci. Technol., vol. 7, no. 4, pp. 449-475, Apr. 1996.

[70] H. Yamada, K. Takashima, K. Ikushima, H. Toida, M. Sato, and Y. Ishizawa, "Magnetic sensing via ultrasonic excitation," Rev. Sci. Instrum., vol. 84, no. 4, pp. 044903, Apr. 2013.

[71] M. Timme, and J. Casadiego, "Revealing networks from dynamics: an introduction," J. Phys. A, vol. 47, no. 34, pp. 343001, Aug. 2014

[72] J. Lv, I. Jeerapan, F. Tehrani, L. Yin, C.A. Silva-Lopez, J.-H. Jang, D. Joshuia, R. Shah, Y. Liang, L. Xie, F. Soto, C. Chen, E. Karshalev, C. Kong, Z. Yang, and J. Wang, "Sweat-based wearable energy harvesting-storage hybrid textile devices," Energy Environ. Sci., vol. 11, no. 12, pp. 3431-3442, Oct. 2018.

[73] R.J. Elble, C. Higgins, and L. Hughes, "Phase resetting and frequency entrainment of essential tremor," Exp. Neurol., vol. 116, no. 3, pp. 355-361, Jun. 1992.

[74] R. Wenzelburger, J. Raethjen, K. Löffler, H. Stolze, M. Illert, and G. Deuschl, "Kinetic tremor in a reachtograsp movement in Parkinson's disease," Mov. Disord., vol. 15, no. 6, pp. 1084-1094, Nov. 2000.

[75] K. Morita, and K. Noguchi, "Crack detection methods for concrete and steel using radio frequency identification and electrically conductive materials and its applications," Proc. SPIE 6932, Sensors and Smart Structures Technologies for Civil, Mechanical, and Aerospace Systems 2008, pp. 69320Q

[76] F. Raeisi, A. Mufti, G. Mustapha, and D.J. Thomson, "Crack detection in steel girders of bridges using a broken wire electronic binary sensor," J. Civ. Struct. Health Monit., vol. 7, no. 2, pp. 233-243, Apr. 2017

[77] A. Sibbald, "Chemical-sensitive field-effect transistors," IEE Proc. I, vol. 130, no. 5, pp. 233-244, October 1983.

[78] G. Tanaka, T. Yamane, J.B. Héroux, R. Nakane, N. Kanazawa, S. Takeda, H. Numata, D. Nakano, and A. Hirose, "Recent advances in physical reservoir computing: A review," Neural Netw., vol. 115, pp. 100-123, Jul. 2019.

[79] S. Scardapane, M. Panella, D. Comminiello, A. Hussain, and A. Uncini, "Distributed Reservoir Computing with Sparse Readouts," IEEE Comput. Intell. Mag., vol. 11, no. 4, pp. 59-70, Nov. 2016.

[80] H. Matsui, Y. Takeda, and T. Tokito, "Flexible and printed organic transistors: From materials to integrated circuits," Org. Electron., vol. 75, pp. 105432, Dec. 2019.

[81] L. Petti, N. Münzenrieder, C. Vogt, H. Faber, L. Büthe, G. Cantarella, F. Bottacchi, T.D. Anthopoulos, and G. Tröster, "Metal oxide semiconductor thin-film transistors for flexible electronics," Appl. Phys. Rev., vol. 3, no. 2, pp. 021303, Apr. 2016.